Characteristics of pebble- and cobble-sized clasts along the Curiosity rover traverse from Bradbury Landing to Rocknest

R. A. Yingst,[1] L. C. Kah,[2] M. Palucis,[3] R. M. E. Williams,[1] J. Garvin,[4] J. C. Bridges,[5] N. Bridges,[6] R. G. Deen,[7] J. Farmer,[8] O. Gasnault,[9] W. Goetz,[10] V. E. Hamilton,[11] V. Hipkin,[12] J. K. Jensen,[13] P. L. King,[14] A. Koefoed,[13] S. P. Le Mouélic,[9] M. B Madsen,[13] N. Mangold,[9] J. Martinez-Frias,[15] S. Maurice,[9] E. M. McCartney,[16] H. Newsom,[17] O. Pariser,[7] V. H. Sautter,[18] and R. C. Wiens[19]

[1]   We have assessed the characteristics of clasts along Curiosity's traverse to shed light on the processes important in the genesis, modification, and transportation of surface materials. Pebble- to cobble-sized clasts at Bradbury Landing, and subsequently along Curiosity's traverse to Yellowknife Bay, reflect a mixing of two end-member transport mechanisms. The general clast population likely represents material deposited via impact processes, including meteorite fragments, ejecta from distant craters, and impactites consisting of shocked and shock-melted materials from within Gale Crater, which resulted predominantly in larger, angular clasts. A subset of rounded pebble-sized clasts has likely been modified by intermittent alluvial or fluvial processes. The morphology of this rounded clast population indicates that water was a more important transporting agent here than at other Mars sites that have been studied in situ. Finally, we identified populations of basalt clasts and porphyritic clasts of undetermined composition by their morphologic and textural characteristics; basalts are confirmed by geochemical data provided by ChemCam.

1. Introduction

[2]   The reconstruction of ancient sedimentary processes and environments from geological data requires basic information about the texture and composition of rocks and soils. For clastic sedimentary materials, important textural parameters include size and shape (roundness and sphericity), sorting (range and proportion of clast sizes), and clast dispersion (distances between clasts). Differences in these parameters within and between clast populations, as well as variations along traverses, or within stratigraphic sections, can help constrain the origin of surficial materials and, thereby, aid in the assessment of past or present environments and habitability.

[3]   Previous landed missions to Mars returned images of sufficient resolution to allow surface clasts in the granule- to cobble-sized range (2–256 mm diameter [*Wentworth*, 1922]) to be characterized in terms of morphology, such that

[1]Planetary Science Institute, Tucson, Arizona, USA.
[2]Earth and Planetary Sciences, University of Tennessee, Knoxville, Tennessee, USA.
[3]Department of Earth and Planetary Science, University of California, Berkeley, California, USA.
[4]NASA Goddard Space Flight Center, Greenbelt, Maryland, USA.
[5]Space Research Centre, Department of Physics and Astronomy, University of Leicester, Leicester, UK.
[6]Applied Physics Laboratory, Laurel, Maryland, USA.
[7]Jet Propulsion Laboratory, California Institute of Technology, Pasadena, California, USA.
[8]School of Earth and Space Exploration, Arizona State University, Tempe, Arizona, USA.

[9]Laboratoire Planétologie et Géodynamique de Nantes, UMR 6112, CNRS and Université de Nantes, Nantes, France.
[10]Max-Planck-Institut für Sonnensystemforschung, Katlenburg-Lindau, Germany.
[11]Department of Space Studies, Southwest Research Institute, Boulder, Colorado, USA.
[12]Canadian Space Agency, St-Hubert, Quebec, Canada.
[13]Niels Bohr Institute, University of Copenhagen, Copenhagen, Denmark.
[14]Research School of Earth Sciences, College of Physical and Mathematical Sciences, Australian National University, Canberra, ACT, Australia.
[15]Geosciences Institute, CSIC-UCM, Facultad de Ciencias Geológicas, Ciudad Universitaria Madrid, Madrid, Spain.
[16]Malin Space Science Systems, San Diego, California, USA.
[17]Institute of Meteoritics, University of New Mexico, Albuquerque, New Mexico, USA.
[18]LMCM, MNHN, Paris, France.
[19]Space Remote Sensing, Los Alamos National Laboratory, Los Alamos, New Mexico, USA.

Corresponding author: R. A. Yingst, Planetary Science Institute, 1700 E. Ft. Lowell, Ste. 106, Tucson, AZ 85719, USA. (yingst@psi.edu)
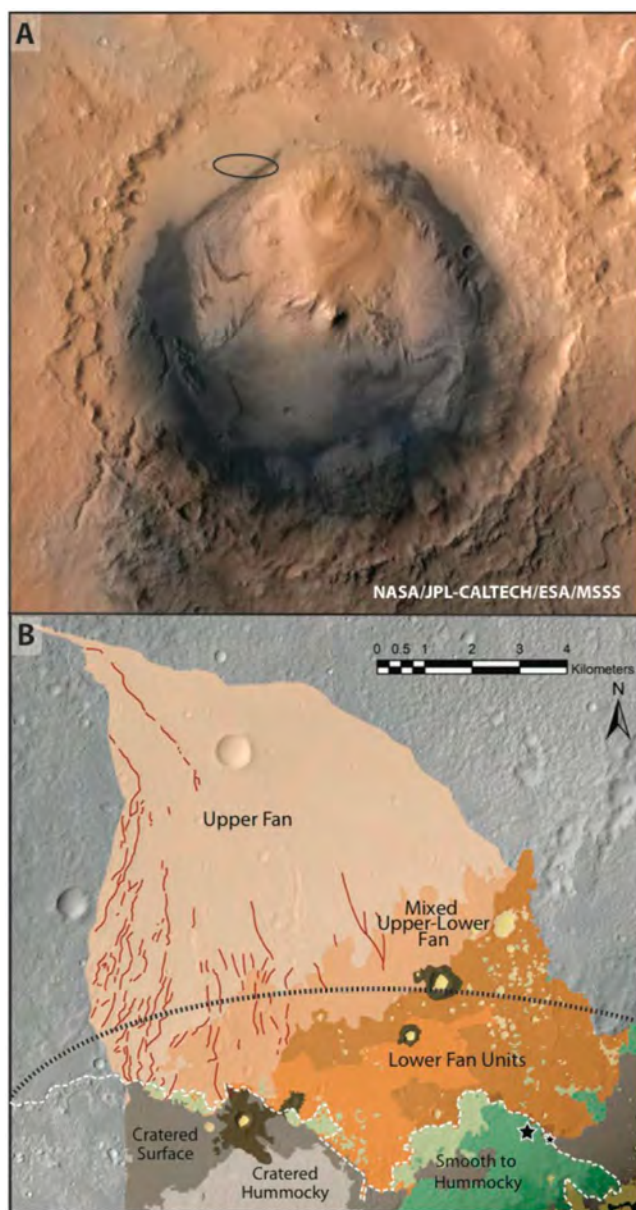
Figure 1. (a) Gale Crater, 5.4°S, 137.8°E, approximately 155 km diameter, with location of the Curiosity landing ellipse. Image combines data from the High Resolution Stereo Camera (HRSC) of the Mars Express Orbiter, the Context Camera (CTX) of the Mars Reconnaissance Orbiter, and color information from Viking orbiter imagery. (b) Map of Peace Vallis area modified from *Sumner et al.* [2013], showing the relative position of the landing ellipse (black dashed line), and the approximate boundary of Bradbury Rise (white dashed line). Peach = upper fan; brown/orange = lower fan; green = smooth to hummocky material. Large star indicates rover landing site, and small star indicates the location of the rover at sol 100.

first-order conclusions could be reached regarding lithology, the origin of rock types, and mechanisms responsible for their emplacement [*Garvin et al.*, 1981a, 1981b; *Basilevsky et al.*, 1999a, 1999b; *Yingst et al.*, 2007]. The Mars Exploration Rovers acquired images across several kilometers of terrain at Gusev Crater and Meridiani Planum, thereby permitting the characterization and analysis of systematic changes in clast characteristics across spatial dimensions [e.g., *Cabrol et al.*, 2006, 2008; *Grant et al.*, 2005; *Grant et al.*, 2006]. These studies provided a template for the procedures we have utilized to investigate clast characteristics along the path traversed by the Curiosity rover during its first 100 sols in Gale Crater.

[4] Orbital studies of Gale Crater have suggested that the Mars Science Laboratory (MSL) landing site lies near the terminus of an alluvial fan system (Peace Vallis fan [*Palucis et al.*, 2013]) that transported potentially large volumes of sediment, via a combination of debris, channelized, and sheet flow, from the crater wall to the interior of Gale Crater. Although the depositional setting of Curiosity's landing site on Bradbury Rise—and its relationship to the Peace Vallis fan—remains uncertain, rover observations of sedimentary conglomerate outcrops in the area indicate the potential for at least local channelized bed load transport. On Earth, fluvial transport within alluvial fan systems is characterized by a decrease in mean clast size from proximal to distal locations, accompanied by an increase in sediment sorting. In addition, clast rounding and sphericity tend to increase with increased length of, or time in, transport. Seeing such changes downslope from the Peace Vallis fan mouth would indicate that the landing site has been covered in sediment transported fluvially from this fan. Characterizing and analyzing changes in clast morphology, size, and sorting have the potential, therefore, to place constraints on both emplacement mechanism and transport direction, thereby providing a means to test hypotheses regarding the relationship of Bradbury Rise sediments to those of the Peace Vallis fan [*Williams et al.*, 2013]. Specifically, understanding of clast morphologies and distributions may constrain whether Bradbury Rise, or its surface, may have been influenced by fluvial activity from the Peace Vallis, and variation. Variations in the expected proximal to distal trends predicted by transport models could lead to a more detailed understanding of both the timing and mechanism of sediment deposition, as well as the relative importance of modification of the substrate by impact and the wind.

[5] Both orbital and surface observations provide evidence for substantial postdepositional modification of the exposed surface by impacts and aeolian erosion. Here we utilize systematic observations to document variation in loose clast populations along the Curiosity traverse from sol 0 at Bradbury Landing to sol 100 at Rocknest, to assess the morphologic characteristics primarily of pebble- to cobble-sized clasts (size ranges used are 2–4 mm granules, 4–64 mm pebbles, and 64–256 mm cobbles [*Wentworth*, 1922]).

2. Geologic Setting

[6] Gale Crater is a large, ~154 km diameter, impact structure near the Martian equator (centered approximately 5°S, 139°E), and straddles the dichotomy boundary that separates heavily cratered highlands to the south and much less cratered lowlands to the north (Figure 1a). After more than 6 years of public discussion and debate in the scientific community, Gale Crater was selected from among a series of candidate sites [*Grant et al.*, 2011; *Golombek et al.*, 2012] as the target with the greatest potential to preserve a historical record of past habitable environments on Mars.

In particular, Gale Crater was determined, based on a variety of orbitally derived geomorphic, mineralogical, and geochemical data sets [*Anderson and Bell*, 2010; *Milliken et al.*, 2010; *Grotzinger and Milliken*, 2012; *Wray*, 2013], to preserve an extensive record of the history of aqueous environments within the crater, over a broad range of depositional environments. Such sites would have potential nutrient and energy sources to support microbial life in the past (see discussion of habitability by *Summons et al.* [2011]).

[7] A complex stratigraphic record of deposition, diagenesis, and erosion in Gale Crater records the potential for aqueous activity across a relatively long duration of time, spanning a critical period in Mars history. Crater counts on ejecta along the southern edge of Gale Crater provide an estimated age of impact in the late Noachian to early Hesperian (or approximately 3.6 Ga) [*Thomson et al.*, 2012]. Preliminary crater counts on geomorphic surfaces within Gale Crater suggest that deposition of the lowermost strata of Aeolis Mons (informally known as Mount Sharp) initiated by at least the early Hesperian [*Thomson et al.*, 2012], and deposition in the region of the landing ellipse may have continued into (or at least may have been exhumed during) the late Hesperian [*Grant et al.*, 2013]. These constraints indicate that deposition of the majority of sediments within Gale Crater occurred during a time interval that may record a critical change in the global climate regime of Mars from relatively warmer and wetter to colder and drier [e.g., *Bibring et al.*, 2006]. Similarly, preliminary mineralogical data derived from the Compact Reconnaissance Imaging Spectrometer for Mars spectra identify a clear stratigraphic succession from iron-aluminum phyllosilicates to possibly (poly)hydrated calcium and magnesium sulfates within the strata of Mount Sharp [*Milliken et al.*, 2010], along with pyroxene and olivine- bearing materials identified by the Thermal Emission Spectrometer and Thermal Emission Imaging System data [*Rogers and Bandfield*, 2009; *Milliken et al.*, 2010], which is consistent with the hypotheses of global-scale climate change. Combined, morphological and mineralogical characters preserved at Gale Crater are substantially more diverse than the morphological support for aqueous activity at Gusev Crater [*Grin and Cabrol*, 1997; *Milam et al.*, 2003], or the dominant mineralogical support for aqueous environments at the Opportunity landing site [*Christensen et al.*, 2001; *Christensen and Ruff*, 2004].

[8] Geomorphic evidence, much of it derived from analysis of medium- (6 m/pixel) and high- (25 cm/pixel) resolution images from the Mars Reconnaissance Orbiter, the Context CTX and High Resolution Imaging Science Experiment (HiRISE) cameras, however, also suggests the potential for an extended time period of aqueous activity within Gale Crater. A rich diversity of structures within the lower units of Mount Sharp [e.g., *Milliken et al.*, 2010], including fine-scale layering containing potential cross stratification [*Malin and Edgett*, 2000], fluvial incision into earlier mound strata [*Malin and Edgett*, 2000], deltaic fan-shaped bodies [*Thomson et al.*, 2008], and an intricate network of mineralized fractures [*Anderson and Bell*, 2010; *Siebach and Grotzinger*, 2013], provides evidence for a range of surface and subsurface aqueous activity. Similarly, within the region of the landing ellipse, numerous inverted channel features [*Anderson and Bell*, 2010], a well-defined alluvial fan

(Peace Vallis fan [*Palucis et al.*, 2013]), and a succession of light-toned layered strata displaying high thermal inertias similar to cemented sedimentary materials elsewhere on Mars [e.g., *Pelkey and Jakosky*, 2002; *Fergason et al.*, 2012] suggest a similarly complex aqueous history.

[9] On 6 August 2012, the Curiosity rover landed on Bradbury Rise (Figure 1b), a smooth-textured, hummocky unit [*Calef et al.*, 2013] located near the distal margin of the Peace Vallis fan [*Palucis et al.*, 2013], where channeled fan deposits interfinger with and transition to light-toned layered strata of Yellowknife Bay [*Sumner et al.*, 2013]. The moderate thermal inertia of Bradbury Rise—consistent with an indurated surface overlain by unconsolidated material [*Fergason et al.*, 2012]—is similar to that of the Peace Vallis fan and is suggestive of common surface characteristics. However, while sedimentary clasts on Bradbury Rise could represent material delivered from an extension of the Peace Vallis Fan, there are no obvious channels forms in the orbital or rover imagery. Detailed mapping of the region has yet to fully resolve the stratigraphic relationships between the units on top of Bradbury Rise and the fan due to aeolian erosion and deflation down to the high thermal inertia units exposed in Glenelg [*Calef et al.*, 2013; *Sumner et al.*, 2013]. Analysis of outcrop materials at and near Curiosity's landing site, however, reveals a variety of scattered pebbles and cobbles, as well as small outcrops of pebble conglomerate that are consistent with bed load transport of sedimentary materials within channelized flow [*Williams et al.*, 2013]. The putative fluvial materials at the surface of Bradbury Rise may represent either an extension of the Peace Vallis fan or a veneer of aqueously transported material deposited over a topographic remnant of previously deposited and eroded material of the Peace Vallis fan system [*Sumner et al.*, 2013].

3. Data Collection

3.1. Clast Survey Campaign

[10] Clast characteristics record primary and secondary processes as a function of time, distance, or both. Documenting variation in clast characteristics from location to location is fundamental to defining the effects of clast transport and to deconvolving the effects of clast emplacement from those of secondary modification. Regular measurements with consistent, well-modeled parameters are required to document the changes along the rover traverse.

[11] Studies of clasts along the Mars Exploration Rover (MER) Spirit traverse utilized images from the "clast survey," an imaging campaign designed to systematically examine clast characteristics as they varied along a traverse [*Grant et al.*, 2005; *Yingst et al.*, 2008]. For Curiosity, we followed an approach similar to MER but use an instrument package and a cadence of observations that is unique to Curiosity.

[12] The Curiosity clast survey data set is composed of image pairs acquired using the Mastcam-34 (M-34) and Mastcam-100 (M-100) mast-mounted cameras. The left Mastcam (M-34) has a 34 mm focal length, a 0.22 mrad/pixel image scale, and an 18.4° × 15° effective field of view (FOV) over 1600 × 1200 pixels of its Kodak KAI-2020 interline transfer charge-coupled device (CCD). The right Mastcam (M-100) uses a similar CCD and has a 100 mm focal length, a 0.074 mrad/pixel image scale, and an effective FOV of

Figure 2. RSVP hyperdrive modeling of clast survey image positions. (a) Position of M-34 image footprint. (b) Position of M-100 image footprint. (c) Combined M-34 and M-100 image footprints. Differences in sighting between M-34 and M-100 images, combined with the angle of viewing for the clast survey results in location of the M-100 image frame near the lower right-hand side of the M-100 image frame.

$6.3° \times 5.1°$ over 1600×1200 pixels [*Malin et al.*, 2010; *Bell et al.*, 2013]. Each Mastcam obtains images through a Bayer pattern of red-green-blue filters and telecentric microlenses bonded onto the CCD [*Bell et al.*, 2012] and can also acquire images through an eight-position filter wheel that provides the ability to obtain additional narrowband images through visible, near-IR, and solar neutral density filters.

[13] Mastcam clast survey images were acquired at a mast orientation of azimuth $120°$, elevation $-45°$ in the rover coordinate frame (where $0°$ azimuth is forward and $0°$ elevation is the nominal horizon), resulting in images aimed toward the ground on the starboard side of the rover near the middle wheel; this geometry is shown in Figure 2. After examining several different potential geometries and field-testing two, this geometry was chosen to best capture a scene as close as possible to the rover, while avoiding rover hardware. In addition, this geometry enables overlap with the near-field portion of the 100 m^2 field of view of the Rover Environmental Monitoring Station (REMS) Ground Temperature Sensor (GTS), allowing cross comparison of these two data sets. Ground temperature provides a measure of the thermal inertia and effective particle size of the substrate, which will eventually be correlated to substrate character. Details of the relationship between local thermal inertias derived from GTS data and clast distributions are described in a companion paper by V. E. Hamilton et al. (Observations and science results from the first 100 sols of MSL REMS ground temperature sensor measurements at Gale Crater, submitted to *Journal of Geophysics Research*, 2013). The viewing angle of this Mastcam pointing yields a working distance of ~2.8 m. A standard subframe of 1152×1152 pixels was chosen for the clast survey images ($14.4° \times 14.4°$ for the M-34, $4.9° \times 4.9°$ for the M-100), with an estimated field of view of 0.71 m and 0.24 m for the M-34 and M-100 cameras, respectively, and a corresponding pixel scale of 0.62 mm/pixel for the M-34 images and 0.21 mm/pixel for the M-100 images.

[14] Surface illumination was also considered in acquiring clast surveys. Surface illumination is a variable correlated with time of day and rover orientations at the time clast survey images are acquired. Based on data from five image pairs captured at different times of the Martian day on sols 24, 30, 39, 41, and 45, we determined that the ideal time to acquire images was in the afternoon, when the sun is at a low-phase angle. A low-phase angle results in images with

enhanced color contrast, which allows rock texture to be better discerned. (Similar low-phase angles in the morning are typically taken up by essential rover engineering activities.) In those instances where it was not feasible to acquire a clast survey at the ideal time, we attempted to acquire a pair as close to that time as possible.

[15] We have attempted to acquire image pairs after every drive, though this has not always been practical or the best use of limited resources. From Bradbury Landing to Rocknest (approximately sols 0–100), clast survey image pairs were acquired on sols 24, 30, 39, 41, 45, 48, 49, 55, and 71. Locations where clast survey pairs were acquired are shown in Figure 3, and image pairs are shown in Figure 4. Clasts imaged as part of the survey represent a subset of unconsolidated surface materials where traversing was possible, practical, and desirable for Curiosity. As such, we expect these surveys to be biased against larger clasts, which were avoided in the interests of rover safety. To ensure that the data set is representative of the clast population along traverse, we also compared clast survey images to other Mastcam images taken on the same, or intervening, sols. Because of differences in resolution, viewing geometry, illumination, and other variables, such comparisons were made on a qualitative basis, only to confirm or refine hypotheses.
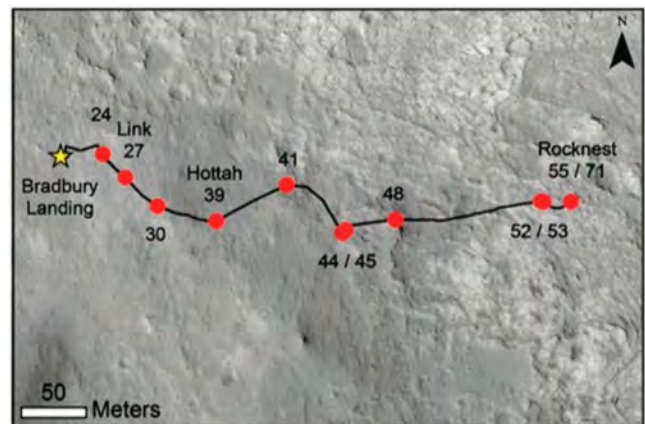

Figure 3. Traverse path of the Curiosity rover from landing to sol 71; HiRISE base image ESP_028335_1755. Sols where clast survey image pairs were acquired are noted as red dots.
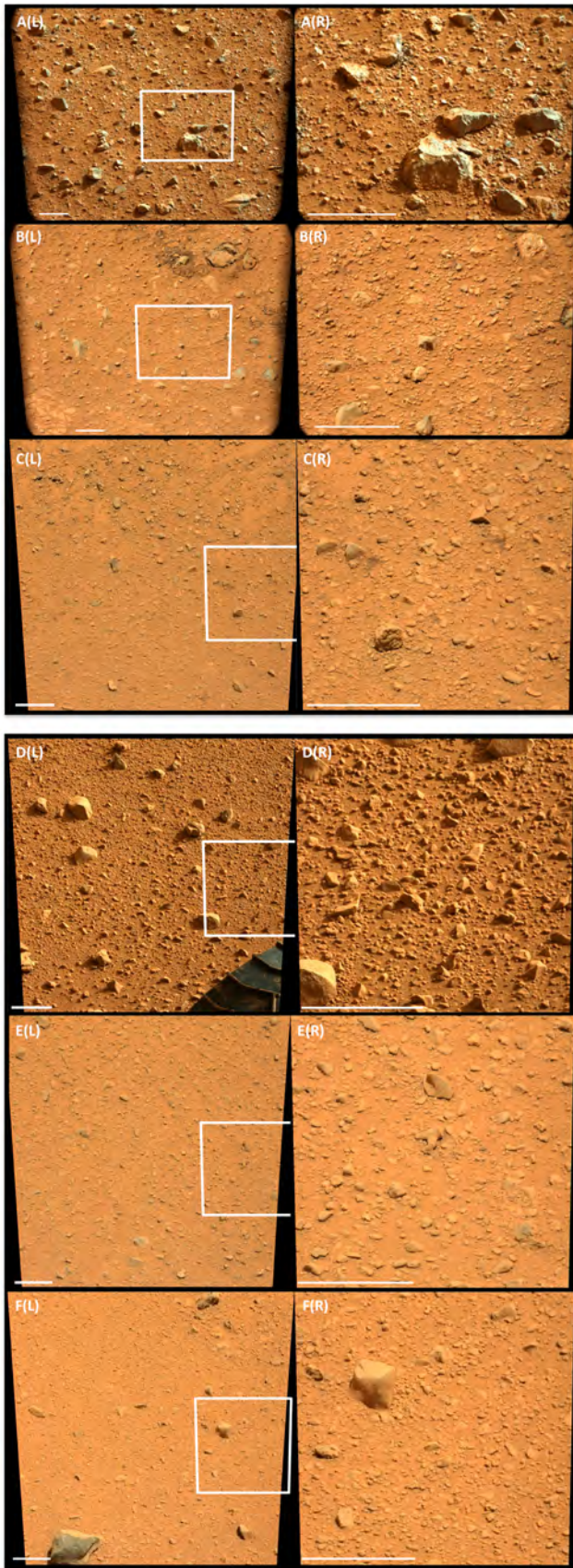
Figure 4

3.2. Other Data Sets

[16] Mastcam clast survey observations were supplemented with a smaller number of images taken by the Mars Descent Imager (MARDI). MARDI acquired images of the landing site, both during and after descent; these first images of the landing site provided a baseline for changes in clast distribution along traverse. The 9.7 mm focal length MARDI camera was designed to acquire video images of Curiosity's descent to Mars but can also acquire images on the ground. MARDI is mounted to the rover body, in a fixed position pointed downward. For imaging on the ground, the $70° × 55°$ frame is oriented with its long axis transverse to the direction of motion. Like the Mastcams, MARDI uses a Kodak KAI-2020CM interline transfer Bayer pattern filter CCD with 1600 by 1200 active 7.4 μm square pixels. The instantaneous field of view (IFOV) is ~0.76 mrad, which provides in-focus pixel scales that range from about 1.5 m at 2 km altitude to 1.5 mm at 2 m altitude and covers a field of view between $2.4 × 1.8$ km and $2.4 × 1.8$ m, respectively. At distances less than 2 m (MARDI is mounted ~70 cm above the ground when the rover wheels are on the surface), out-of-focus blurring increases at the same rate that spatial scale decreases, resulting in resolutions poorer than 1.5 mm/pixel for images acquired on the ground. Practical resolution is also reduced by the accumulation of dust on the camera lens, presumably acquired during landing [*Malin et al.*, 2009].

[17] When available, we also utilized Remote Microimager (RMI) images from the ChemCam system to confirm hypotheses or refine classification of clasts. The ChemCam RMI is part of the ChemCam Mast Unit. The system incorporates a 110 mm diameter Schmidt Cassegrain telescope which is dually used for the laser-induced breakdown spectroscopy and the RMI. A small portion (~10%) of the light received by the telescope is directed to an Atmel $1024 × 1024$ pixel CCD integrated into a flight spare camera from the European Space Agency Rosetta mission [*Maurice et al.*, 2012]. The field of view of the RMI is 20 mrad, i.e., a pixel scale of 20 μrad/pixel; however, the actual image resolution is 50 μrad, limited somewhat by optics rather than being pixel limited [*Le Mouélic et al.*, 2013; *Langevin et al.*, 2013]. It is thus the highest-resolution remote imaging camera on MSL. Unfortunately, due to the wide aperture, the RMI acquires images with a narrow depth of focus of only 23 mm at 3 m distance, or 90 mm at 6 m. At these same distances, the field of view is only slightly larger at 68 and 135 mm, respectively. A total of 248 RMI images

Figure 4. Clast survey image pairs acquired from Bradbury Landing to Rocknest on (a) sol 24 (0024ML0119001000E1 and 0024MR0119001000E1); (b) sol 30 (0030ML0133000000E1 and 0030MR0133000000E1); (c) sol 39, predrive (0039ML 0176000000E1 and 0039MR0176001000E1); (d) sol 39, postdrive (0039ML0179000000E1 and 0039MR017900 1000E1); (e) sol 41 (0041ML0188000000E1 and 0041MR 0188001000E1); (f) sol 45 (0045ML0207000000E1 and 0045MR0207001000E1); (g) sol 49 (0049ML0225000000E1 and 0049MR0225001000E1); (h) sol 55 (0055ML0255 000000E1 and 0055MR0255001000E1); (i) sol 71 (0071ML 0495000000E1 and 0071MR0495001000E1); and (j) distribution of pebble- to cobble-sized clasts for each sol. All images above were rectified as described in the main text and scale bars are all 100 mm. The clast survey image pair for sol 48 is shown in Figure 7.
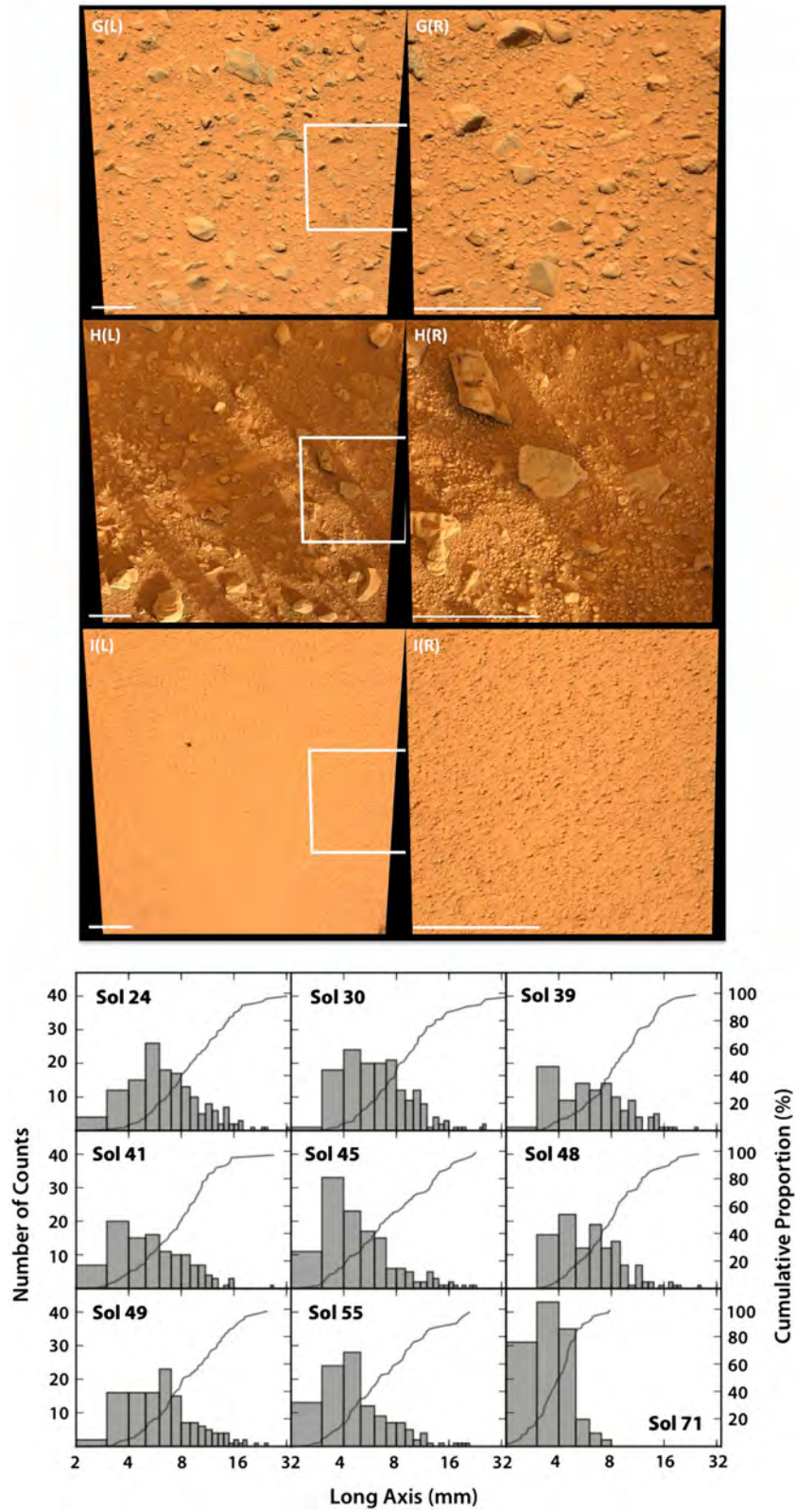
Figure 4. (continued)

was acquired for approximately 40 targets in the first 90 sols of the mission, most of the images supporting ChemCam Laser-Induced Breakdown Spectrometer (LIBS) compositional observations. The benefits of high resolution, and the ability to acquire images remotely (rather than through deployment of the rover turret, as is required for Mars Handlens Imager
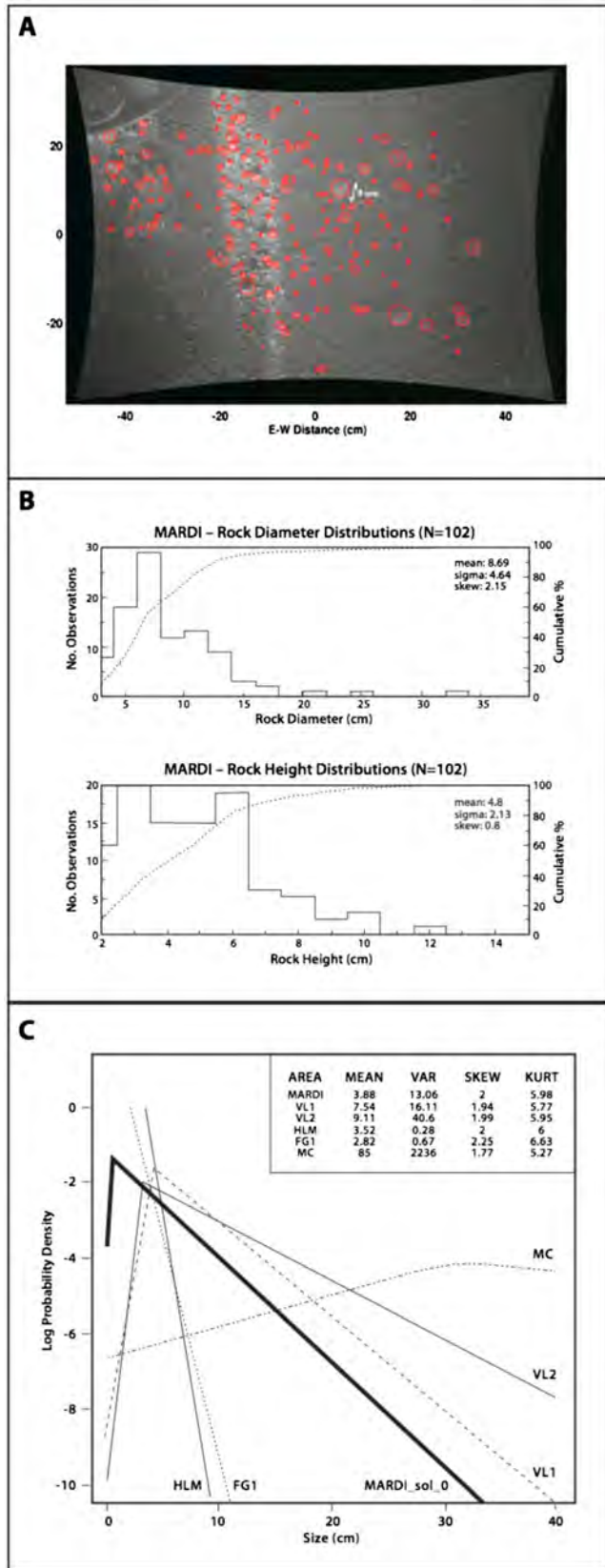
(MAHLI) images [*Edgett et al.*, 2012; M.E. Minitti et al., MAHLI (Mars Handlens Imager) at the Rocknest sand shadow: Science and science-enabling activities, submitted to *Journal of Geophysical Research-Planets*, 2013.], however, have resulted in substantial use of RMI images to analyze and understand rock texture and to make inferences regarding rock lithology.

4. Methodology

4.1. Mastcam Image Processing

[18] All standard Mastcam clast survey images were rectified (i.e., the images are given the same linear length scale everywhere in the image) to simplify measurement of clast morphology and size distribution. Further characterization of clasts in selected survey images utilized stereo meshes generated by the Operations Product Generation Subsystem (OPGS) Team at the Jet Propulsion Laboratory.

4.2. RMI Image Processing

[19] The ChemCam RMI images were corrected for standard electronic and geometric effects [*Dufour et al.*, 2010], and partially for radiometric effects [*Langevin et al.*, 2013], using both ground and in-flight calibrations. This processing resulted in gray scale images, which were slightly sharpened or stretched to enhance textural information.

4.3. Analysis of MARDI Images

[20] We performed geometric and radiometric calibration on ~0.5 mm/pixel resolution MARDI descent images from sol 0 (We note that the calculated effective resolution on the surface is 1.5 mm but the computed pixel scale resolution is 0.51 mm. Here we use the pixel scale projected from the nominal height, which is 0.51 mm.) We attempted to measure clast size distributions from a range of altitudes but only made reliable (cal/Val checked) measurements for pretouchdown data on the single image acquired at ~41 m above the final landing surface. These ranges are based on the reconstructed temporal sequence that includes the spacecraft clock and the phased array radar.

Figure 5

Figure 5. Data derived from MARDI sol 0 images. (a) Example of corrected MARDI sol 0 frame (#1008) acquired approximately 1 min after touchdown of the Curiosity rover in Gale Crater. Red circles indicate 211 particles for which diameters and heights were measured using methods developed for use with Viking lander images [*Garvin et al.*, 1984]. (b) Distribution of 102 measured clasts from entire MARDI Sol 0 pretouchdown imaging sequence using log hyperbolic distribution analysis methods, showing the differences between the gravel-sized population and the coarser fraction. The top panel shows mean clast diameter statistics; the bottom panel shows clast heights. (c) Log hyperbolic distribution analysis of the composite (merged) MARDI sol 0 clast size data, plotted in bold. Earth reference data include the near-rim ejecta from Meteor Crater (MC), as well as Halema'umau' explosive (phreatic) ejecta from Hawaii (HLM), and flood gravels from Iceland (FG1). Both Viking lander sites (VL1 and VL2) are also plotted for comparison. Note the similar slope of the coarse "tail" of the MARDI sol 0 distribution to that of VL1.

[21] We chose uniform areas of study assuming the mean height of the camera above the surface (as fit by a tangent plane to make it horizontal). For pretouchdown data, we utilized the reconstructed timing from the entry, descent, and landing (EDL) profile to develop a mean height above the surface; for posttouchdown data, preflight calibration data allowed us to establish a mesh, from which we measured the gravel-sized clasts. When compared to values calculated along traverse, values calculated for MARDI images were consistent to better than 5%.

[22] From a subset of images, we constructed a composite distribution representing clasts from ~0.5 to 82 cm. This was used to measure a representative population of clasts to facilitate size distribution analysis using classical sedimentary petrology methods, including the log hyperbolic distribution [*Folk*, 1974; *Bagnold and Barndorff-Nielson*, 1980; *Garvin et al.*, 1984].

4.4. Analysis of Sorting From Clast Survey Images

[23] Each Mastcam clast survey image pair was used to determine the range and distribution of clast sizes. These data were then used to calculate the degree of sorting. We performed a grid count on rectified Mastcam images, following the methods of *Bunte and Abt* [2001]. A 10–20 mm grid was placed over each image and thus allowed us in an unbiased way to select individual clasts for further investigation. We measured the longest visible axis of the clast located at each grid intersection point (this method may underestimate clast size if the longest axis is obscured). If the clast was too small to measure, we marked it as "fines." The smallest clast size that we were able to resolve in the images was ~0.7 mm, so the fine fraction is represented by all sedimentary particles less than 0.7 mm in diameter. We determined the percentile values for D_x, where D is the clast diameter and x is the percent of the surface finer than x. We also calculate the corresponding φ values, where φ is defined as

$$\phi_i = -\frac{\log(D)}{\log(2)} \quad (1)$$

[24] Sorting (σ), which measures the spread in the data from the median clast size, was calculated using the definition of *Folk and Ward* [1957]:

$$\sigma = \frac{\phi_{84} - \phi_{16}}{4} + \frac{\phi_{95} - \phi_5}{6.6} \quad (2)$$

[25] There are several ways in which sorting is calculated in the literature (i.e., the *Inman* [1952] sorting coefficient or a second moment analysis [*Bunte and Abt*, 2001]), but *Folk and Ward* [1957] include a broader range of the cumulative size distribution curve into their sorting analysis and recognize seven categories of sorting, from very well ($\sigma < 0.35$) to extremely poor ($\sigma > 4$). This finer division of sorting is important for data sets, such as those collected of the Martian surface, where little is known about the origin and history of the sediments.

[26] As a check to this methodology, and to facilitate presentation in more than one format, stereo-image algorithms developed by the Operations Product Generation Subsystem (OPGS team) at JPL were applied to overlapping images to produce *XYZ* maps (in local-level coordinates). These *XYZ* maps were constrained to the areal extent of the overlapping data sets, with the resolution limited by the lowest resolution camera (Mastcam left-eye, M-34), using a grid by number scheme described by *Bunte and Abt* [2001] to ensure an unbiased selection of clasts for further analysis. From *XYZ* maps coregistered with M-100 image data, we used customized software to mark up individual clasts and extract corresponding *XYZ* data as point clouds. Clast size distributions and shapes were extracted from these point clouds (shapes restricted to the visible parts of clasts). A lower limit for the size of clasts analyzed in this way was five points in the point cloud, or roughly the same number of pixels, which corresponds to a physical minimum size of about 1 mm.

4.5. Analysis of Clast Morphology From Clast Survey Images

[27] In addition to analysis of size and sorting, we utilized the methodology of *Yingst et al.* [2008] to estimate clast size, shape (sphericity, or how closely a clast profile resembles a sphere), roundness (a measure of corner sharpness), and texture (qualitative variation from a flat surface at scales smaller than the corners). Elements of texture also include the size, morphology, and dispersion of grains within an individual clast, where the term "grain" is limited to features observed within clasts. Such measurements are best suited to clasts within the pebble- to cobble-sized range, because two-dimensional clast analysis typically overestimates clast characteristics at smaller sizes at low resolution (35–150 μm/pixel) and results in inconsistent size and shape characteristics [*Friday et al.*, 2013].

[28] The greatest constraint affecting shape analysis was image resolution. Resolution is defined as a theoretical measure of the smallest object that can be identified by a single pixel; in practice, however, a candidate clast must be much larger than a single resolved pixel to make realistic inference of size and shape. Even greater resolution is required to assess textural characteristics. The size of a single clast, for example, may be ascertained to within 10–20% given a long axis that is at least 4–5 pixels in length (~1 mm long-axis in M-100 images); however, a substantial coating of unconsolidated "dust," as is observed on a number of clasts, increases the practical limit for determination of size to ~10–20 pixels long axis. Similarly, characteristics such as shape and sphericity depend on resolving the smallest "lobe" or protuberance of a clast, and roundness requires even more detailed knowledge of the outline of a clast—5–10 pixels per edge or corner, translating to at least 100 pixels (~21 mm in M-100 images) long axis for angular clasts [*Yingst et al.*, 2008]. For more qualitatively assessed characteristics such as surface texture and color, the resolution required to make a reasonable analysis depends to a certain extent on the clast itself; varicolored clasts would require greater resolution to make an accurate assessment of individual components, for example.

[29] In this study, we chose a conservative minimum of 20 pixels long axis for measuring clast size and a minimum of 100 pixels long axis for quantitatively measuring other morphologic characteristics such as shape or roundness. These values translate to approximately 12 and 60 mm long axis for measuring size and shape, respectively, from M-34 images and 4.2 and 21 mm long axis for measuring size and shape, respectively, from M-100 images. This is a larger

Figure 6. Example of surface pavement, comprised of 2–4 mm diameter clasts. Sol 39 (postdrive) M-100 clast survey image 0039MR0179001000E1.

minimum than the 20 pixel limit that was adopted by *Williams et al.* [2013] for roundness assessment of clasts in and around conglomerate outcrops. This is because many clasts along Curiosity's traverse are more angular than those found near conglomeratic outcrops; clasts with greater angularity require finer resolution to sufficiently resolve and measure corners and edges [*Barrett*, 1980; *Benn*, 2004; *Yingst et al.*, 2008]. Thus, although we measured size and sorting of all clasts >0.7 mm, shape was assessed on clasts greater than ~12 mm, and roundness data were measured only on clasts greater than ~21 mm; we caution that when making any comparison between these and other data sets, the size fraction being considered must be consistent.

[30] All clasts fitting our defined criteria were measured for size and shape, including sphericity and roundness, using the methodology of *Yingst et al.* [2008]. We also qualitatively assessed clast texture (how the surface of a clast varies from a perfectly flat surface at scales smaller than its corners and angles). We used the greater coverage of M-34 images primarily for measuring distribution and sorting of clasts, particularly medium-sized pebbles to cobbles; the higher resolution of M-100 images was best for measuring shape, roundness, and texture. Additionally, because these two image data sets overlap (Figure 2c), we were able to compare our observations for consistency, using a subset of clasts imaged by both cameras. Clasts were not included in our analyses if they were truncated by the image border, were partially draped by unconsolidated material, or had outlines that were otherwise obscured (e.g., by shadowing or other clasts).

5. Observations

5.1. Landing Site Data

[31] As a first point of comparison, we analyzed clast size distribution and shape from the MARDI images acquired

during the entry, descent, and landing (EDL) sequence on sol 0. The MARDI imaging sequence provides a nadir-looking view of the landing site at lower and lower altitudes (finer and finer resolution), thereby revealing regional and local context for surface materials, including clast abundance at various sizes. MARDI sol 0 images show an armored surface dominated by relatively equant gravel-sized clasts. Figure 5a illustrates an image acquired during the sol 0 posttouchdown sequence [*Grotzinger et al.*, 2012].

[32] Two things are evident from sol 0 data. First, there is a paucity of boulders in the immediate landing area (in the MARDI field of view there are only three clasts are larger than 256 mm diameter). This can be seen graphically in Figure 5b. The mean clast size in MARDI images is 87 mm, with only a few clasts larger than 200 mm (and only one clast as large as 800 mm). We note that the MARDI viewed area is many times smaller than those typically studied by previous studies that focused on boulder distribution at the landing site [*Golombek et al.*, 2012], and at much finer spatial sampling (HiRISE allows feature identification resolution of about 0.9m, compared to better than 9 cm at ~41m altitude via MARDI). Thus, the intrinsic sampling scale (and hence feature identification scales) is very different.

[33] Second, the narrow aspect of the MARDI hyperbolic distribution reflects a high degree of winnowing of the observed population. Figure 5c illustrates the log hyperbolic distributions for MARDI sol 0 (surface), VL-1 [*Moore et al.*, 1987], and the Icelandic Flood Deposit "FG1" reported in *Malin* [1988], plotted in log-log space [*Garvin et al.*, 1981a, 1981b; *Malin*, 1988, 1989]. The general "shape" of the MARDI sol 0 distribution closely mimics that of the Iceland flood gravel deposits (FG1), albeit with its mean displaced to a finer clast size (from ~2 cm to ~1 cm). That is, the slope of the tail of the line representing MARDI data (one of the asymptotic flanks) has a slope that very nearly mimics the FG1 line (to within 5%). Such displacements can reflect selective winnowing during deposition, or dispersive pressures associated with high-energy emplacement. In this case, impinging of high-pressure exhaust from the lander's engines on the Martian surface reactivated substantial amounts of surface material, resulting in localized dispersal of dust and even small clasts [*Schieber et al.*, 2013], so that the landing itself may have resulted in in situ winnowing of surface materials, thereby directly impacting the surface clast distribution.

5.2. Size and Sorting

[34] Based on results from the methods described in section 4.4, clast survey images, as well as other Mastcam images acquired along traverse, Bradbury Landing, and surrounding regions on Bradbury Rise, are covered by a pavement of granules, pebbles, and boulders [e.g., *Williams et al.* [2013]], as shown in Figure 6. About 30–40% of the surface is covered in this pavement of granules and small pebbles, and this pavement appears in all but the first clast survey image pair, taken on sol 24. Depending on the location, 0–10% of the surface is covered by large pebbles to cobbles. Boulders are rare. The distribution of clast sizes for each clast survey is shown graphically in Figure 7. To allow for comparison with *Williams et al.* [2013], we also include clast size data excluding the fine fraction.

[35] To assess sorting on a site-by-site basis, point clouds were derived from local-level *XYZ* maps (described in
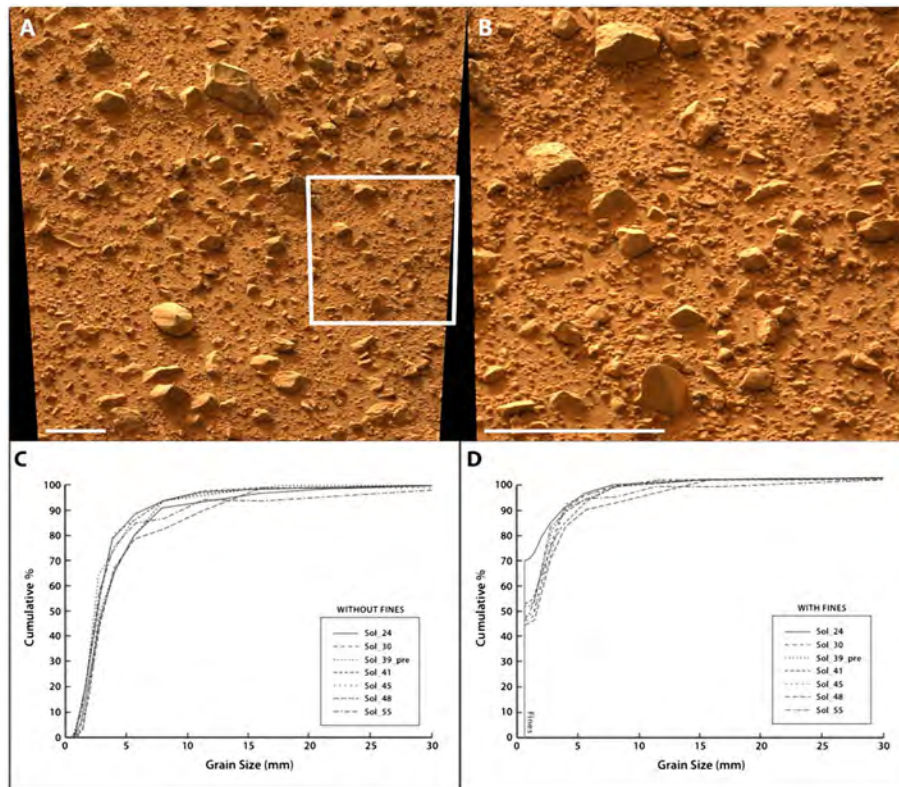
Figure 7. Clast distribution. (a) Sol 48 M-34 image 0048ML0217000000E1, rectified, with location of M-100 marked; scale bar 100 mm; (b) sol 48 M-100 image 0048MR0217001000E1, rectified, scale bar 100 mm. Cumulative frequency grain size plots for seven of the clast survey images taken along Curiosity's traverse are also shown, including sol 48, where the fine-grained fraction is (c) excluded and (d) included.

section 4.4) and ellipsoids were fitted to these using principal component analysis. From these, we derived the distributions of clast sizes in terms of the lengths of the major axis of the fitted ellipsoids. The resulting clast size distributions for each sol are shown in Figure 4j.

[36] The distribution found on sol 71 varies most from that of other sols, in that there is a complete lack of clasts larger than about 8 mm, making the distribution strongly skewed toward smaller clasts. About 90% has sizes below 5 mm. The clast size distribution found on sol 45 is also somewhat skewed toward smaller clasts, with the majority ~2–5 mm, with a cumulative proportion of larger clasts rising almost linearly with the logarithm of the long axis of the clasts. The distribution of sol 24 has a peak at clasts between 4 and 5 mm with counts falling off rapidly away from this size range. By comparison, the distributions found on sols 39 and 41 are flatter, with a much more equal distribution among sizes and the cumulative proportion rising only slowly at small sizes. Distributions of sols 30, 48, and 49 all have a relative large evenly distributed block of clasts between 2 and 8 mm, and a correspondingly regular s-shaped cumulative proportion as this rises with size. The area covered by the clast survey pair acquired on sol 49 (Figure 4g) is exactly the same as that acquired on sol 48 (Figure 7) but was acquired at different local solar times in very different illumination conditions. These different conditions affect the stereo product to a great enough extent that both image pairs are retained. In the oblique lighting angle resulting from a late afternoon observation time (Local True Solar Time

(LTST) 16:43), clasts larger than 12 mm were harder to identify (or to ascertain that they were indeed lying loosely on the surface), whereas the contours of clasts of this size range were easier to identify in lighting conditions near noon (LTST 12:07). This difference does not seem to give rise to a strong change in the measured size distribution, but there are small differences in details of the distribution, which we attribute to small differences in observation conditions between the two sets of lighting as described above rather than just statistical fluctuations. Additionally, as the selection of pixels to include in analysis of each clast was done by hand, we expect slight variations in the actual pixel values selected, and thus the individual clast sizes.

[37] The largest clast counted on the grid as part of the sorting analysis of clast survey images was ~55 mm diameter (Table 1); this is smaller than the largest boulders captured in MARDI sol 0 descent images, but both data sets confirm that clasts in the cobble or boulder size range are relatively rare. This is also consistent with the visual inspection of Mastcam images of the surrounding landscape—a few boulders scattered here and there. The population of clasts smaller than cobbles is consistent along the traverse, with a mean clast size ranging between 1.0 and 3.7 mm depending on whether or not fines are included in the analysis.

[38] Clasts imaged by the clast survey campaign are not well sorted. Statistically, if the fines population is included in the count, the images represent a poorly sorted substrate (based on *Folk and Ward* [1957]), with σ values ranging between 1 and 2 (see Table 2) If the fines fraction is excluded from the

Table 1. Number of Clasts Counted Per Image[a]

Sol #	No. Clasts (# Fines)	Maximum Clast Size (mm)	Minimum Clast Size (mm)
24	552 (370)	30.5	0.7
30	313 (136)	34.6	0.9
39_pre	202 (99)	18.7	1.2
41	186 (93)	18.6	1.0
45	140 (63)	34.2	1.0
48	135 (56)	23.8	0.9
55	130 (57)	55.5	0.8

[a]Number of clasts counted per image, as well as the maximum and minimum clast size values for each survey. In the first column, the total number of points counted as fines (defined as <0.7 mm) is included in parenthesis. In order to have statistically significant values, we performed at least 100 counts per image, per *Wolman* [1954].

population, surface clasts are moderately sorted, with σ values between 0.7 and 1 (see Table 3). The number of larger clasts (greater than ~21 mm) varies from site to site, but these larger clasts are a small percentage of the total number of clasts.

5.3. Morphology

[39] A representative example of clast populations along traverse is shown in Figure 7. For this image pair, approximately 30% of the surface is covered by granules and small pebbles, as revealed by the higher-resolution M-100 image; about 5–10% is covered by pebble- to smaller cobble-sized clasts (20–100 mm long axis), as seen in the M-34 image. The largest clast in this pair is ~135 mm across; only two clasts 100 mm across or more are visible. For clasts larger than 100 pixels across, sphericity is estimated at 0.76, and roundness is angular to subangular.

[40] For all clast surveys acquired up to Rocknest, clasts have an average sphericity of 0.76. On Earth, sphericity values of 0.70–0.77 are commonly associated with terrestrial environments dominated by intermittent, high-energy transport [e.g., *Howard* [1992]; *Miall* [1970]]; clasts modified by sustained transport processes typically have higher maximum sphericities (0.71–0.83 [*Krumbein and Sloss*, 1963]). Some differences are found with clast properties in cold dry environments relative to wet environments [e.g., *Bockheim*, 2010], but without a priori knowledge of the past environment of Gale Crater, it is not possible to evaluate this further.

[41] Throughout the clast survey images, clasts range from rounded to very angular, though the majority of very coarse pebbles to boulders (86% of those >21 mm as noted in section 4.5) are subangular to very angular. Subangular to very angular roundness values are consistent with little

modification of original clasts, or modification by inefficient rounding mechanisms. However, along Bradbury Rise, roundness also appears to correlate broadly with clast size. A distinct population of very fine to coarse pebble-sized clasts exists that displays a pronounced rounding [*Williams et al.*, 2013]. Such pebbles occur as detritus near the base of conglomerate outcrops, but they are also observed in varying amounts elsewhere along traverse as well.

[42] For example, Figure 8 shows clast size frequency at three locations: immediately adjacent to the Hottah conglomerate outcrop (sol 39), 1 m away, and 40 m away (a representative example of the pervasive rock pavement). Clasts in the first and last localities show distinct peaks recording different values for the most prevalent clast size (pebble and cobble, respectively) at the two locations. By contrast, the clasts in intermediate distance from Hottah show a pair of peaks, with one matching the size distribution of pebbles within (and eroding from) the conglomerate outcrop and the other matching the regional surface pavement. This bimodal distribution is consistent with the mixing of rounded pebbles, presumably from fluvial transport, with a pervasive, coarser rock pavement.

6. Classification Based on Macroscale Clast Characteristics

[43] In addition to using clast characteristics to provide fundamental information regarding the emplacement mechanisms of Martian surface materials, macroscale clast characteristics can also be used to organize surface materials into discrete classes based on similarities in size, shape, roundness, and macrotexture. Such categorization provides a critical first look at the diversity of surface materials, from which more detailed analyses (e.g., ChemCam, RMI, and MAHLI) can be targeted.

[44] Clast survey data from the first 100 sols of the Curiosity mission result in three distinct morphologic classes; these classes typify the most commonly occurring morphologies observed along traverse. These clast types provide statistically sufficient data and display sufficiently distinct morphology and macrotexture to make reasonable inferences with regard to lithology. We also note some particularly distinct clast morphologies that represent more unusual components. We consider this initial organization of classes as a baseline for further investigation into understanding the range, and potential origins, of surface materials within Gale Crater. The process of data analysis and integration of results across instruments is still in its early stages; we fully expect these classes to evolve as analysis and understanding matures.

Table 2. Percentile Values for Each Image in φ Units, Including Fines[a]

Sol #	φ_5%	φ_16%	φ_50%	φ_84%	φ_95%	Mean	σ	Sorting
24	0.96	0.88	0.62	−1.65	−2.77	−0.05	1.20	poor
30	0.94	0.82	−0.67	−1.85	−2.68	−0.57	1.22	poor
39_pre	0.94	0.94	−0.25	−1.80	−2.72	−0.37	1.24	poor
41	0.95	0.84	0.50	−2.10	−2.64	−0.25	1.28	poor
45	0.94	0.82	−0.70	−1.81	−2.70	−0.56	1.21	poor
48	0.94	0.81	−0.84	−2.24	−3.58	−0.76	1.45	poor
55	0.94	0.81	−0.35	−1.85	−3.35	−0.46	1.32	poor

[a]σ = sorting coefficient as defined in equation 2. Values of σ between 1 and 2 are considered poorly sorted based on the *Folk and Ward* [1957] sorting coefficient (defined above).

Table 3. Percentile Values for Each Image in φ Units, Excluding Fines[a]

Sol #	φ_5	φ_16	φ_50	φ_84	φ_95	Mean	σ	Sorting
24	−0.25	−0.70	−1.63	−2.70	−3.77	−1.68	1.03	poor
30	−0.55	−0.77	−1.43	−2.32	−3.25	−1.51	0.80	moderate
39_pre	−0.52	−0.73	−1.36	−2.40	−3.47	−1.50	0.86	moderate
41	−0.52	−0.81	−1.59	−2.65	−3.25	−1.68	0.87	moderate
45	−0.55	−0.97	−1.46	−2.29	−3.21	−1.57	0.73	moderate
48	−0.58	−0.90	−1.64	−3.13	−3.81	−1.89	1.05	poor
55	−0.04	−0.56	−1.26	−2.02	−4.36	−1.28	1.02	poor

[a]σ = sorting coefficient. Values of σ between 1 and 2 are considered poorly sorted and values between 0.71 and 1 are considered moderately sorted (based on the *Folk and Ward* [1957] sorting coefficient). When only looking at the coarser size fractions, the degree of sorting increases slightly as there is less spread in the grain size data. Most gravel fluvial systems typically range from 0.5 to 2 when using a φ-based sorting coefficient [*Bunte and Abt*, 2001].

[45] Over 90% of rocks fall into three types: Type 1 (referred to in earlier works as Coronation type after the first rock target of that type), Type 2 (previously noted as porphyritic type), and Type 3 (previously called Link type, after the Link target) [*Yingst et al.*, 2013]. Representative examples of each of these classes are shown in Figure 9. Other distinctive rocks include Wolverine, Douglas, Blanchet, and rocks with features such as pits or voids, and those with ventifacted surfaces. Rock names throughout this work are not approved by the International Astronomical Union, but have been used informally by the MSL team and are thus used here for consistency and convenience.

6.1. Type 1 Clasts
6.1.1. Macroscale Features

[46] Clasts of this type are gray, with or without a light tan patina or coating. Along the traverse, the long axis of these clasts varied broadly from ~5 to 30 mm. Despite differences in size, all examples are angular to subangular, with flat or slightly curved faces ending in sharp to slightly rounded edges. The surface texture visible in clast survey images is typically smooth and lacks striations or other features that may represent penetrative layering. Smooth surface textures can be rough and knobby at the millimeter scale, suggesting a generally fine-grained, homogeneous nature. Surfaces of these clasts are variably smoothed by the wind, and faceting resulting from wind erosion is common. Type 1 clasts are a common clast type, comprising 60–80% of coarse pebble- to cobble-sized clasts, depending upon location. Examples of this type include Coronation and Mara targets (Figures 9a and 9b). The Jake Matijevic mugearite float rock [*Stolper et al.*, 2013] also falls within this clast type. Most clasts that can be identified as ventifacts are Type 1 clasts.

6.1.2. Microscale Features

[47] Analysis of RMI images of Type 1 clasts supports macroscale inferences of broadly homogeneous grain size. Figures 10a and 10b show RMI images of Coronation and Mara, respectively. Both these images confirm the sculpted macroscale morphology and the relative homogeneity of grains/crystals that comprise the rocks. At RMI resolutions, we are able to distinguish discrete differences in internal grain size (millimeter-scale mixture of dark and light-toned grains in Coronation; 2 mm scale mixture of dark and light-toned grains in Mara). In these two samples, grain size, combined with potentially different weathering potential of light- and dark-toned grains, appears to be the controlling factor in determining surface smoothness of the macroscale facets.

6.2. Type 2 Clasts
6.2.1. Macroscale Features

[48] A noteworthy rock class first documented on Mars by Curiosity is the porphyritic type [*Wiens et al.*, 2013]. Several clasts were observed with light-toned, bladed, or polygonal inclusions (up to ~5mm × 2mm) in a gray-toned matrix. Clasts average 50–100 mm long axis and are commonly angular to very angular. The surface texture of the clasts is commonly hackly (or jagged). Figure 9c shows an example of this clast type imaged on sol 24. In addition, grain textures of Peacock Hills, as revealed by RMI images, indicate that
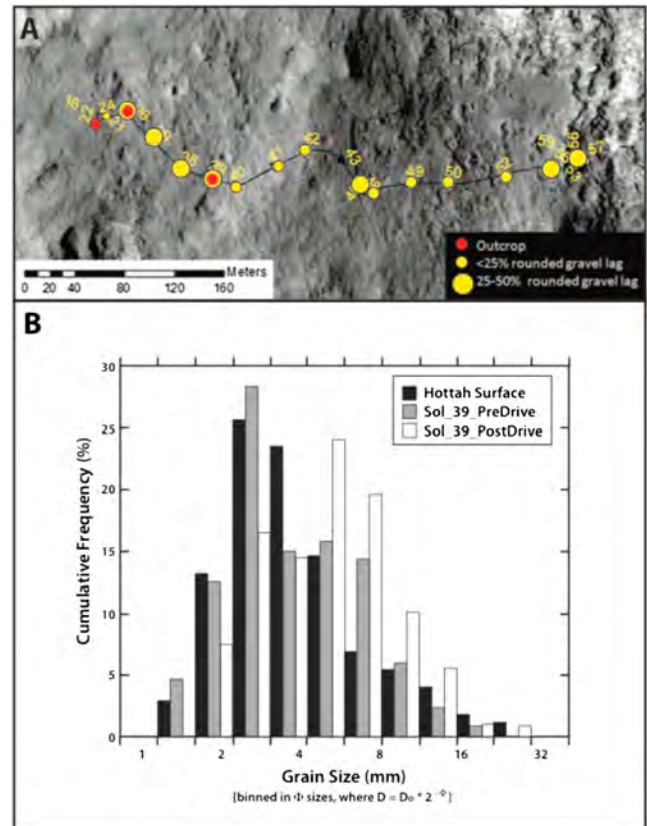

Figure 8. (a) Relative percentage of surface covered in rounded pebbles in Mastcam surface images; the location of conglomerate outcrops is shown in red for comparison; (b) cumulative frequency plot of binned data (in φ grain size) for surface immediately adjacent to Hottah surface (black), surface near Hottah (~1 m distance, gray), and ~40 m from Hottah (white).
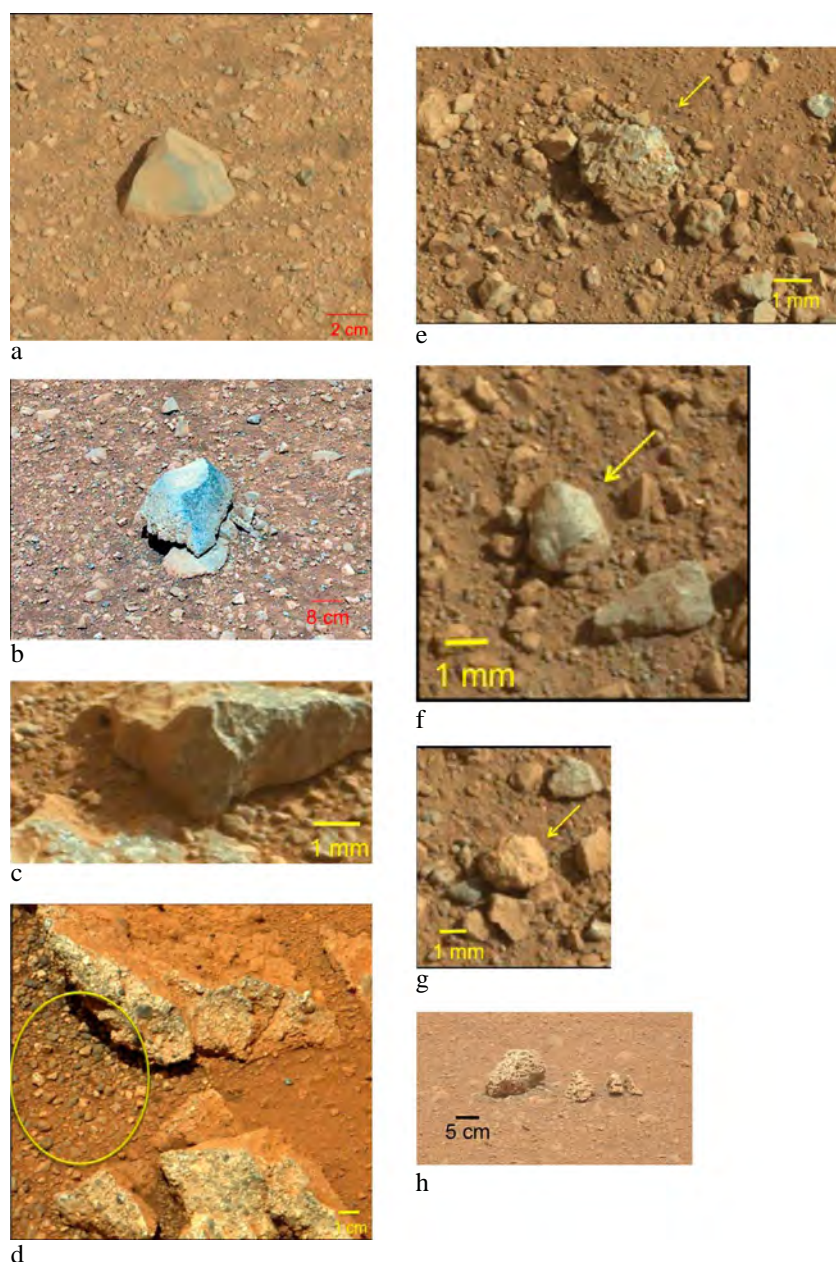
Figure 9. Examples of clast types: (a) Type 1 clast Coronation, M-34 image acquired sol 3; (b) Type 1 clast Mara, M-34 image acquired sol 2, adjusted for color levels; (c) Type 2 clast, M-100 image acquired sol 24; (d) Type 3 clasts around Link outcrop (arrow), M-100 image acquired sol 27; (e) Blanchet (arrow), M-34 image acquired sol 3; (f) Wolverine (arrow), M-34 image acquired sol 3; (g) Douglas (arrow), M-34 image acquired sol 3; and (h) example of pitted/vuggy clast, M-100 image acquired sol 20.

this rock may also be porphyritic. Some porphyritic-type clasts are found in groups of similar clasts. Although relatively rare (or perhaps not always easy to resolve), these clasts differ substantially from those observed at other rover sites on Mars [e.g., *Garvin et al.*, 1984; *Yingst et al.*, 2007, 2008; *Wiens et al.*, 2013].

6.2.2. Microscale Features

[49] Peacock Hills, a clast near Goulburn outcrop, is the only putative Type 2 clast for which an RMI image has been acquired (Figure 10c). The Peacock Hills RMI image reveals a number of very large light and dark grains (to >1 cm), leading us to classify this rock as Type 2. However, there

are differences between the grains in Peacock Hills and those in other porphyritic rocks, so this must be considered a preliminary classification, pending more information.

6.3. Type 3 Clasts

6.3.1. Macroscale Features

[50] Type 3 clasts (Figure 9d) are loose clasts commonly found in the vicinity of conglomerate outcrops such as Link and Hottah, often littering the surface surrounding outcrops of conglomerate. Clasts vary in tone, can be equidimensional to somewhat elongate, and are composed of subrounded to well-rounded constituent particles [*Williams et al.*, 2013].
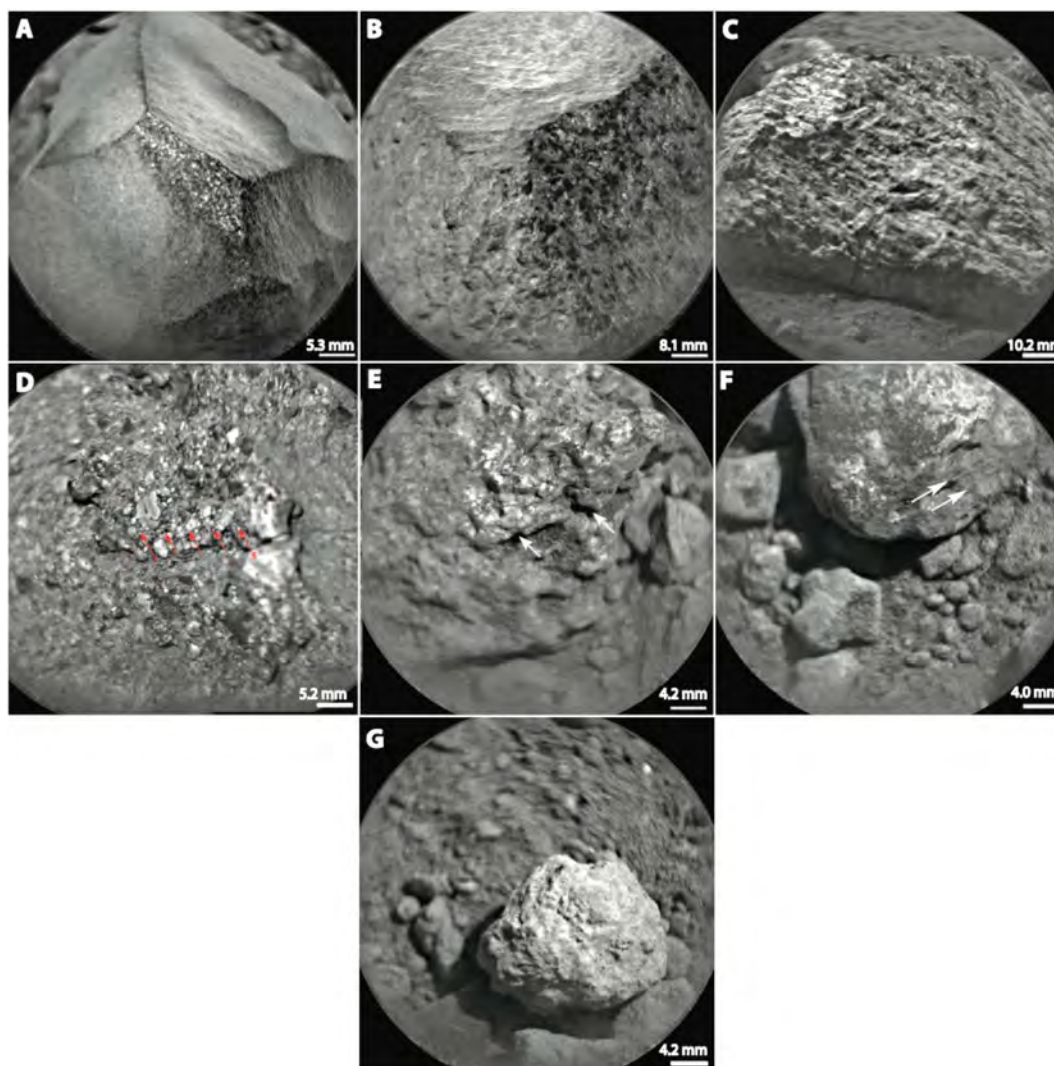
Figure 10. RMI images of type clasts: (a) Coronation; (b) Mara; (c) Peacock Hills; (d) Link; (e) Blanchet, showing irregular voids with overhanging pendants (white arrows); (f) Wolverine, showing potential layering along one rough surface (white arrows oriented with potential layering); and (g) Douglas.

Individual constituent particles are commonly released via weathering and comprise a significant component of the clast population in some areas along traverse, including near Rocknest.

6.3.2. Microscale Features

[51] RMI images were not acquired of loose clasts associated with Type 3 materials; RMI images of Link, however, reveal details regarding the relationship between rounded to subrounded pebbles and matrix materials. Within Type 3 clasts and parent material, larger clasts are supported by a variety of finer-grained components that are typically heterogeneous in tone, angular to rounded, and range from a few millimeters in diameter to below RMI resolution (Figure 10d).

6.4. Other Clasts

6.4.1. Blanchet

[52] Blanchet (Figure 9e), Stark, and similar clasts are mottled in color, with or without patches of a tan patina or dust coating. The surface texture is very rough and distinctively characterized by millimeter-scale irregular voids and pendants. In the single available RMI image, pendants are seen

to be quite rounded, and voids are deep enough that finer-grained (<100 μm) sediments or sediment clumps have collected in them (Figure 10e). Clasts range from very angular to rounded and equidimensional in shape. The bladed voids and pendants are consistent with the possible chemical weathering of soluble mineral constituents within the matrix of these clasts.

6.4.2. Wolverine

[53] Wolverine (Figure 9f) and similar clasts are dark, have a blue-green mottled tone, and are commonly coarse grained. Clasts are ~5–20 mm long axis and range from angular to rounded. Some clasts display a rough, platy surface texture that may indicate potential layering. This potential layering is seen at higher resolution in RMI images of Wolverine (Figure 10f), though the texture only appears along dust-covered surfaces. Other Wolverine surfaces appear rounded in RMI images, with areas of higher reflectance that may indicating polishing. Though first grouped with the rock Peacock Hills, RMI images revealed the difference in internal grain size and texture indicating a difference in lithology.

6.4.3. Douglas

[54] Douglas (Figure 9g) and similar clasts are uncommon along traverse. They are small and light-toned, often with a coating of dust. Rounded to subrounded in shape, most clasts in this class are ~5–15 mm long axis, with a very rough, knobby surface texture. The single RMI image of the type clast of this class (Douglas, Figure 10g) shows millimeter-sized bumps and knobs that may represent individual constituent grains or consolidated clumps of material.

6.4.4. Pitted/Vuggy Clasts

[55] Clasts described as "pitted" or "vuggy" are relatively gray and are distinguished by large (1–5 mm) vuggy or vesicular texture (we refer to the generic definition of the term "vug" as a small cavity in a rock and make no assumption as to whether the cavity is filled with mineral material). These clasts have a distinctive void-covered surface mantled by a light-toned patina or coating of dust. Voids are circular or elongated concave-outward ellipsoids, averaging 0.5–1.5 mm long axis. Clasts tend to be ~20–40 mm long axis and are commonly angular to subangular, with some flat facets and rounded edges and corners. First identified on sol 20 (Figure 9h), these clasts also appear near the Rocknest area and along the traverse toward Shaler. The distinctive texture of these clasts may be derived from volcanically derived vesicles, actual primary vugs, or it could represent a conglomerate in which the matrix was more solidly cemented than the clasts, allowing the clasts to be released during weathering. An impact origin for the vugs is possible where impact processes have mobilized volatile materials that form vugs when they escape from the rock.

6.4.5. Fractured Clasts

[56] Some clasts appear to have been broken or fractured in situ. One example is seen from the M-100 clast survey image acquired on sol 24 (Figure 11). Such clasts could form from in situ mechanical weathering, such as by thermal shattering along planes of weakness. The existence of some planar fractures along which there is no obvious evidence of shearing motion, the mineralogical detection of salts (e.g. sulfates, which would expand and fracture rocks as they come out of solution), and the large day/night temperature variations observed during the first 100 sols, all would support fracturing by mechanical weathering.

6.4.6. Ventifacts

[57] Ventifacts are rocks abraded by windborne particles (generally sand) [e.g., *Laity*, 2009; *Laity and Bridges*, 2009], and clasts of any type may be considered ventifacts. On Earth, ventifacts are identified by a combination of unique morphological features and distinctive millimeter- to centimeter-scale surface textures. Equivocal textures include pits, for which abrasion is only one of several formation mechanisms; a combination of fine lineations (or striations) and elongated pits, flutes, and grooves are more definitive. These textures are typically aligned, with the long axes providing a proxy for the average direction of near-surface winds above the saltation threshold. Distinctive macroscale morphological features include distinct facets, which at their upper boundaries are commonly separated from other facets by sharp keels and which, where there has been soil deflation, terminate at their bases adjacent to nearly vertical sills. The Pathfinder and MER missions showed that ventifacts are common on Mars [*Bridges et al.*, 1999; *Sullivan et al.*, 2005; *Greeley et al.*, 2006; *Thomson et al.*, 2008] and attest

to the role that windblown sediment plays in sculpting the surface over time.

[58] Similarly, in Curiosity's traverse from Bradbury Landing to Rocknest, numerous rocks display surface textures consistent with aeolian abrasion; these features can be observed in a variety of image scales, from Mastcam, to MAHLI, to RMI. Although a detailed study of ventifacts seen by MSL is underway [*Bridges et al.*, 2013], we note several qualitative attributes from our preliminary investigation. Although ventifacts are distributed throughout the traverse along Bradbury Rise, most appear to be concentrated in the landing zone and in the Rocknest area. This distribution may reflect selective bias from the greater number of clasts examined in these regions. All of the diagnostic textures noted above are observed, with several examples displaying multiple characteristics of wind erosion. The most notable of these examples is Jake Matijevic, which displays faceting, elongates flutes along faces, and has a distinct basal sill indicative of soil deflation (Figure 12).

7. Correlation With ChemCam Results

[59] The chemistry of the clasts observed between Bradbury and Rocknest was provided exclusively by ChemCam. Targets included clasts of all sizes and a number of different textures. One conglomerate targeted by ChemCam, "Link," is discussed elsewhere [*Williams et al.*, 2013]. Small loose pebbles were in many cases hit by ChemCam when simply targeting the ground in the early part of the mission because of the ubiquity of small clasts near Bradbury. Such targets include Beaulieu sol 33, points 2, 3, 4 (Figure 13a), Kam sol 43, points 1, 7 (Figure 13b). The corresponding sizes (max diameter) are Beaulieu 3.6, 3.0, and 5.0 mm, and Kam 2.1 and 2.1 mm, respectively. These clasts do not show any evidence of veins or particular textures, presumably due to their small size. Several slightly larger clasts were imaged by the ChemCam RMI but without corresponding LIBS analyses; as noted in section 6.4, these include Douglas (13 mm), Blanchet (~40 mm, similar to Stark), and Wolverine (layered, ~30 mm). Clasts of sizes 50 mm and larger were targeted for both LIBS and RMI. These include Stark, Coronation, Mara, Thor Lake, Pekanatui, Taltheilei, and Natkusiak.

[60] Compositions are discussed elsewhere for the small pebbles [*Meslin et al.*, 2013] and larger clasts [*Wiens et al.*, 2013; *Sautter et al.*, 2013]. Overall, many of the small clasts, including the ones in Beaulieu and Kam and also within the conglomerate Link display relatively high Si, Al, and alkali compositions consistent with the presence of abundant feldspars; this represents compositions distinct from those measured at MER and Viking sites. Note that *Meslin et al.* [2013] used a broad definition of "pebbles" that included points with high Si in the soils. While the proximal occurrence of both rounded pebbles and conglomerate outcrops suggests that the pebbles are weathering products of the conglomerates, the composition of Link is distinctly different [*Williams et al.*, 2013; *Wiens et al.*, 2013; *Ollila et al.*, 2013] from all other targets sampled by ChemCam, particularly in the trace elements, with more than twice as much Rb (>100 ppm) and Sr (>1000 ppm) than any other observations in the first 100 sols, although many of the pebbles are also enriched in these elements compared to the average soil
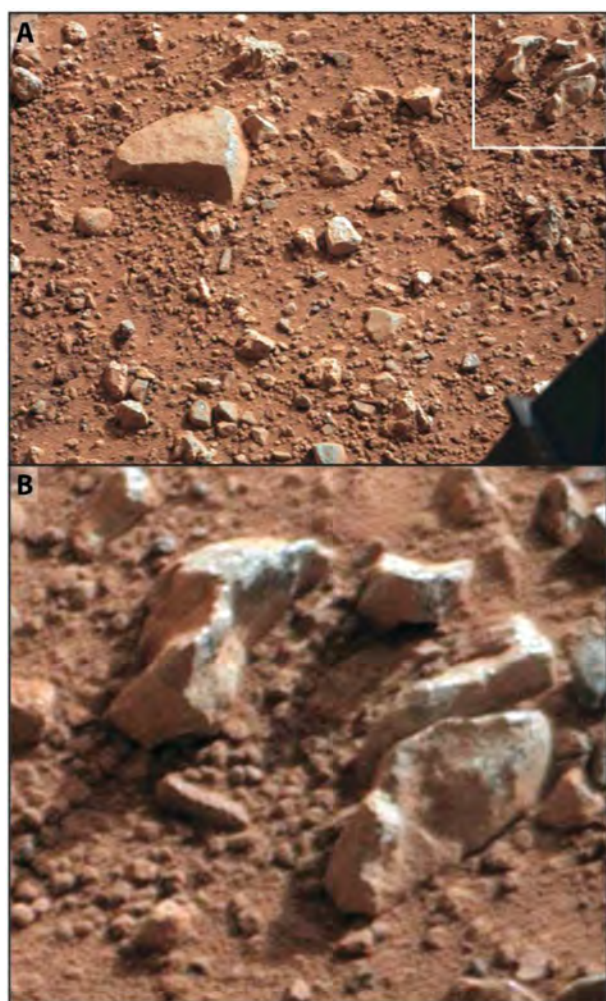
Figure 11. Probable in situ rock breakdown in sol 24 M-100 clast survey image. M-100 image 0024MR0119000000E1 is shown on top and a closeup of this image on the bottom.

[*Ollila et al.*, 2013]. The distinct composition of Link may suggest a source region difference from other pebbles on Bradbury Rise.

8. Comparison of Clasts to Those at Previous Landing Sites

[61] The sites of Viking 1 and 2 [*Garvin et al.*, 1981a, 1981b], Mars Pathfinder (MPF) [*Yingst et al.*, 2007], and MER Spirit [*Yingst et al.*, 2008] have been subjected to systematic assessments of clast morphology. The intermediate sphericity and relatively high angularity of clasts at these sites have been interpreted to derive from a single lithology of volcanic origin, modified to a small extent by ballistic impact and aeolian abrasion. Fluvial processes have been invoked only for the MPF site, and only for boulders, which have higher sphericity and are subrounded and imbricated. For clast sizes larger than ~21 mm, the percentage of clasts assessed as very angular to sub angular at the Curiosity site is nearly identical to that of other sites on Mars: 64%, compared to 62% (MER Spirit [*Yingst et al.*, 2008]), 62% (MPF [*Yingst et al.*, 2007]), 64% (V1), and 76% (V2 [*Garvin et al.*, 1981a]).

[62] Rounded pebbles observed by Curiosity, however, are distinct from the dominantly angular to subangular shape for clasts of a similar size at other sites on Mars, as shown in Figure 14. This figure shows qualitative roundness values for clasts in the area around the conglomerate outcrop Link, as representative of the small, rounded pebble population that occurs to a greater or lesser extent all along traverse (described in section 5.3). These are comparable in roundness to that observed for the Mars Pathfinder site, the Spirit traverse, and from distal alluvial fan facies in the Atacama Desert, Earth. While the Spirit and Pathfinder sites show the sharp peak at subangular values that is common for a population subjected to high-energy emplacement and little subsequent wear [*Yingst et al.*, 2007, 2008], the rounded pebble population at Gale Crater shows a flattened profile in Figure 14, which has as its maximum subrounded and rounded values. Based on this comparison, the most rounded clast populations at Gale Crater are more similar to terrestrial fluvial deposits than other Martian landing sites.
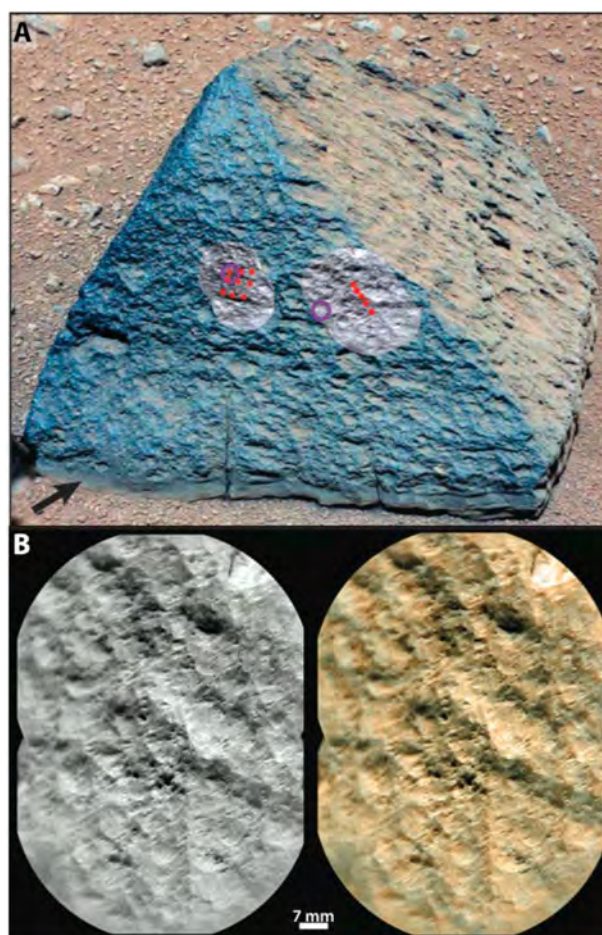

Figure 12. Jake Matijevic ventifact. (a) Mastcam 100 image with superposed RMI mosaics shown in gray scale; red dots are the location of LIBS spots. (b) The rightmost RMI mosaic is enlarged in at left, with merged Mastcam color at right [*Le Mouélic et al.*, 2013]. Jake Matijevic has the most prominent abrasion textures seen in the first 100 sols, with a distinct keel at its crest (arrow), penetrating flutes, elongated pits, lineations, and a basal sill.
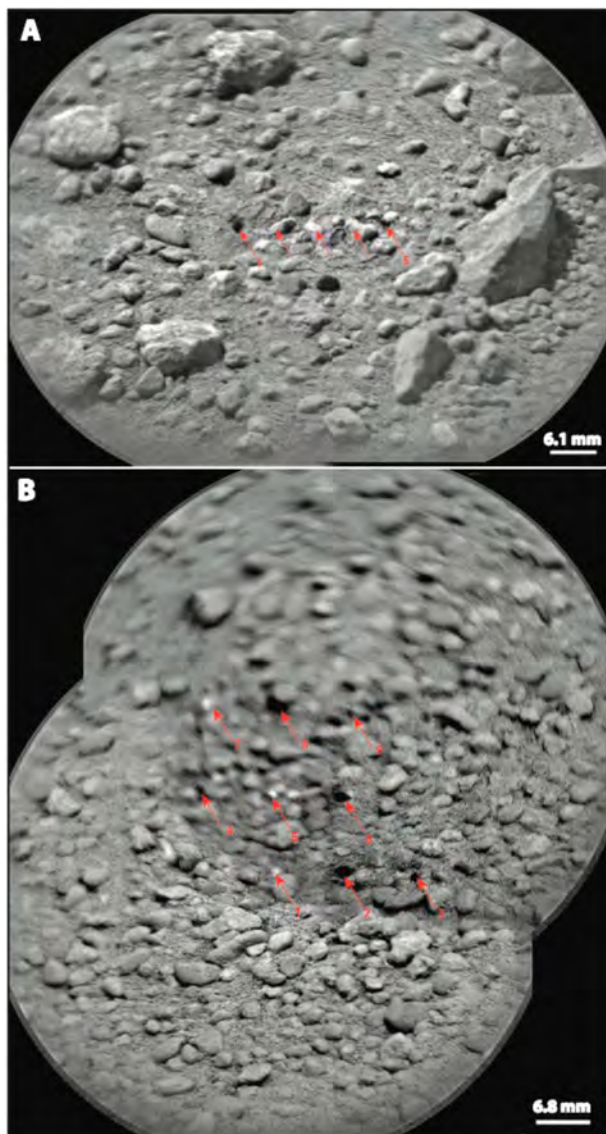
Figure 13. RMI mosaic images of (a) Beaulieu and (b) Kam.

9. Interpretations and Discussion

[63] The findings of this study are as follows:

[64] 1. The similarity between the log hyperbolic distributions for MARDI sol 0 "VL-1" and the Icelandic flood deposit "FG1" is consistent with the interpretation that some aspect of fluvial transport could be a factor—along with modification during EDL—in the development of the well-sorted, armored surface revealed at progressively higher-resolution MARDI images.

[65] 2. The fine to coarse granules and pebbles (~2–20 mm in size) are inferred to be poorly to moderately sorted at the landing site and along the traverse based on σ values and analysis of sol 0 descent images. The number of larger clasts (>20 mm) varies from site to site. The larger clasts are also more angular, suggesting less abrasion during transport. We interpret the smaller clasts to be representative of regional clast emplacement mechanisms, such as aeolian, alluvial, or possibly fluvial processes. The large clasts likely reflect stochastic modification of the surface by rare local events such

as impacts. *Presley and Christensen* [1997] demonstrated a relationship between particle size and thermal inertia that can be used to infer particle size from thermal inertia [e.g., *Fenton et al.*, 2003]. Although this relationship is defined based on samples having uniform particle size and inertias $<350 \, \mathrm{J \, m^{-2} \, K^{-1} \, s^{-1/2}}$, thermal inertia is a nonunique parameter and the thermal inertia associated with a material having a single, intermediate particle size also can be the apparent inertia exhibited by mixtures of smaller and larger particles [e.g., *Pelkey and Jakosky*, 2002]. Properties such as cementation [e.g., *Piqueux and Christensen*, 2009] and lateral and vertical heterogeneity [*Putzig and Mellon*, 2007a, 2007b] also affect apparent thermal inertia, but detailed consideration of these factors is beyond the scope of this work (see Hamilton et al. (submitted manuscript, 2013) for a detailed discussion of thermal inertia along Curiosity's traverse in the first 100 sols). The moderate nighttime inertias typical of the Gale landing ellipse (250–410 $\mathrm{J \, m^{-2} \, K^{-1} \, s^{-1/2}}$ at 100 m/pixel) were predicted by *Fergason et al.* [2012] to represent an indurated, possibly layered, surface with the presence of unconsolidated material, where the lower inertias correspond to effective particle sizes of 175–415 μm and the intermediate inertias suggest sizes of 415–1110 μm. As shown in section 5.2, measured clast size distributions along Curiosity's traverse exhibit little variation (Figure 7). Orbital thermal inertia values over the area of the traverse do not vary significantly either, ranging from ~370 to 400 $\mathrm{J \, m^{-2} \, K^{-1} \, s^{-1/2}}$ [*Fergason et al.*, 2012]. Based on extrapolation [*Fenton et al.*, 2003] of the *Presley and Christensen* [1997] relationship, the measured nighttime thermal inertias along Curiosity's traverse suggest either a uniform or an effective mean particle size of 2–4 mm. Particle sizes measured from Mastcam clast survey images are not uniform but have a relatively consistent particle size distribution with mean values from 1.0 to 3.7 mm. Thus, the predictions from thermal inertia are, at a broad level, consistent with the measured particle size distributions. Comparisons of MSL-derived thermal inertias, observed
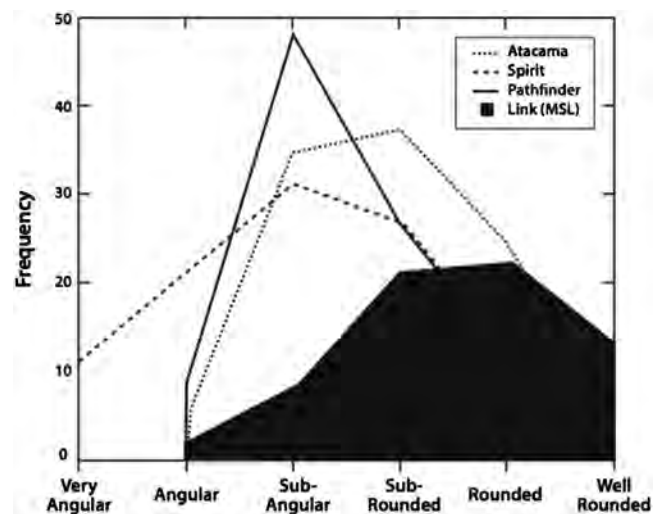

Figure 14. Relative roundness of clasts around the target Link compared to similarly sized clasts from other surface observations on Mars from Pathfinder and Spirit. Data for a distal alluvial fan deposit in the Atacama Desert are also included for terrestrial comparison.

particle size distributions, and local terrain are described in more detail by Hamilton et al. (submitted manuscript 2013).

[66] 3. For coarse pebble- to boulder-sized clasts, sphericity and roundness are generally consistent with intermittent, high-energy transport, such as impact. Pebble-sized clasts, however, may be divided into two distinct populations. Whereas most clasts are subangular to very angular, consistent with little modification, there is a distinct, pebble-sized population that shows consistently higher rounding (subrounded to rounded). Rounded pebbles in the conglomerate outcrops are interpreted as fluvially transported sediment [*Williams et al.*, 2013]; by extension, we infer that most rounded clasts of similar size observed along traverse also reflect significant fluvial abrasion and suggest that surface water flows may have been widespread over Bradbury Rise. Further work is needed to obtain detailed quantitative shape and roundness data along the entire traverse to determine the extent of this rounded pebble population.

[67] 4. Clast morphology is rarely diagnostic of parent lithology. However, certain textural features can provide insight into clast genesis. For example, the morphology of cavities within clasts may constrain both the range of potential lithologic origins and the environmental circumstances under which they formed. Cavities formed by entrapment of gas bubbles (either within volcanic or sedimentary rocks) are often equant to elongate in shape, with a distinctly concave-outward outline. Despite the range of lithologies in which such features form, their presence implies volatile release [e.g., *Furniss et al.* [1998] and *Pollock et al.* [2006] for sedimentary rocks). Cavities resulting from erosional loss of components, on the other hand (e.g., removal of sedimentary clasts or preferential dissolution of a crystalline element) may or may not have these morphologic characteristics (see *Yingst* [2009] for documented examples of these cavity morphologies at the submillimeter to millimeter scale). In another example, although macroscale features such as surface smoothness appear to reflect a combination of grain size and the homogeneity of grain sizes, they do not uniquely reflect compositional lithologies. Similarly, the presence of discrete surface striations, as modified by surface weathering, is likely to reflect fundamental differences in lithology (either differences in grain or crystal size or changes in the hardness of different components); micro-scale imaging is likely to be critical in determining potential origins. Porphyryclasts, on the other hand, can often be inferred from the presence of a hackly surface texture, especially when accompanied by clear color differentiation. We note unique, diagnostic, or otherwise interesting textures and other data for each clast type and make inferences regarding rock history below. For other types, there is currently insufficient evidence to warrant classification with respect to lithologic origin:

a. Coronation is identified in clast survey and other images as fine grained, with Mara being slightly coarser grained. The smooth surface texture, flat facets, and undulating breakage/wear pattern are common characteristics in basalt fragments, and we interpret them as such, with varying grain sizes as revealed in RMI images. ChemCam data confirm that both Coronation and Mara are basaltic but also indicate that the different textures are due to underlying differences in lithology. Coronation is an alkali basalt with aphanitic texture, while Mara is porphyritic

with at least one millimeter-sized, dark olivine grain visible in RMI images.

b. The textures of Type 2 clasts are most consistent with either a volcanic or impact origin. Consistent aspect ratios and sizes of the white inclusions indicate that these are likely individual crystals (i.e., phenocrysts that are magmatic in origin) rather than rock/mineral fragments that would result from impactite and fallback breccia. The combination of crystal form and color leads us to interpret these as pyroxene and/or plagioclase phenocrysts. It is most likely that the white mineral is pyroxene based on abundant light-colored pyroxene phenocrysts in the Martian shergottite meteorites (e.g., Los Angeles, NWA1460, and EETA79001). Plagioclase cannot be ruled out, but it is less abundant in the Martian meteorites and it is commonly shocked to form maskelynite that is black in hand specimen. Like those meteorites, the matrix of the Type 2 clasts may be composed of plagioclase, pyroxene, trace phases, ± olivine, ± glass (volcanic and/or impact), and ± alteration/hydrous phases. A volcanic interpretation would also be consistent with the high abundance of basalts previously characterized on Mars [e.g., *Gellert et al.*, 2006; *Ming et al.*, 2008; *Sautter et al.*, 2013; *Stolper et al.*, 2013; *Schmidt et al.*, 2013; *Wiens et al.*, 2013]. We note that Peacock Hills is differentially weathered, with the top appearing less weathered than the bottom and the far left side appearing very weathered, so that the layering texture stands out clearly. If a similar target is available, acquiring LIBS data for both types of surfaces would be crucial to classifying this rock more definitively and in understanding how weathering has influenced rock texture.

c. As noted above, we interpret these rounded clasts to be fluvially transported clasts [*Williams et al.*, 2013]. Some rounded pebbles may record deposition that never experienced induration, while others likely have eroded from conglomerate outcrops such as Link. We infer that rounded clasts near conglomerate outcrops are derived by the physical disaggregation (and/or dissolution) of matrix components within adjacent conglomerate outcrops. ChemCam composition of pebbles give various compositions (from mafic to felsic) consistent with the various tones observed consistent with multiple rock sources [*Meslin et al.*, 2013].

[68] 5. The close similarity to analog ventifacts on Earth strongly suggests that the Martian examples experienced wind abrasion over prolonged timescales [*Laity and Bridges*, 2009]. West of the Rocknest/Pearson region, the lack of prominent sand and drift deposits, as seen both from the rover and in HiRISE images, as well as the presence of basal sills and perched rocks in other areas, indicates that the local terrain has undergone deflation. Therefore, sand probably passed through this area in the past, even if not abundant today. This suggests that the ventifacts are fossil features that are not currently undergoing active abrasion. The Rocknest ventifacts are also likely relict, as the armored sand shadow likely reflects the long-term stabilization of aeolian accumulation (Minitti et al., submitted manuscript, 2013).

10. Conclusions

[69] Observations of clast characteristics permit preliminary analysis of emplacement mechanisms for surface materials and provide the opportunity to assess the contributions of secondary processes (e.g., impact emplacement, wind erosion) in modifying the original substrate surface. Clast angularity, along with the stochastic distribution of large clasts, even when smaller clast sizes show similar distribution, suggest the potential for emplacement via impact. Smaller clasts are more rounded and commonly associated with pebble conglomerate outcrops with sedimentary features (e.g., pebble-rich layers), indicative of fluvial transport and clast modification. Comparison of the characteristics of pebble-sized clasts with similarly-sized clasts at other Martian landing sites indicates that water was a more important transporting agent here than at other Mars sites that have been studied in situ. Additionally, clasts represent a more diverse lithology than has been previously sampled at other Martian sites examined in situ. Unique textures (e.g., porphyritic) indicate that the history of this site (or the localities represented by the clasts delivered to it) is lithologically complex.

[70] The overprinting of various factors on clast morphology will likely make definitive identification of lithologic classes and thus rock origin difficult; nevertheless, a systematic study of all properties described above may lead to the emergence of useful criteria for classification of clasts of different genesis.

References

Anderson, R. B., and J. F. Bell III (2010), Geologic mapping and characterization of Gale Crater and implications for its potential as a Mars Science Laboratory landing site, *Mars*, *5*, 76–128, doi:10.1555/mars.2010.0004.

Bagnold, R. A., and O. E. Barndorff-Nielson (1980), The pattern of natural size distributions, *Sedimentology*, *27*, 199–207.

Barrett, P. J. (1980), The shape of rock particles, a critical review, *Sedimentology*, *27*, 291–303, doi:10.1111/j.1365-3091.1980.tb01179.x.

Basilevsky, A. T., W. J. Markiewicz, N. Thomas, and H. U. Keller (1999a), Morphologies of rocks within and near the Rock Garden at the Mars Pathfinder landing site, *J. Geophys. Res.*, *104*, 8617–8636.

Basilevsky, A. T., W. J. Markiewicz, N. Thomas, and H. U. Keller (1999b), Morphology of APXS-analyzed rocks at the Mars Pathfinder landing site, *Sol. Syst. Res.*, *33*, 170–186.

Bell, J. F., III, M. C. Malin, M. A. Caplinger, M. A. Ravine, A. S. Godber, M. C. Jungers, M. S. Rice, and R. B. Anderson (2012), Mastcam multi-spectral imaging on the Mars Science Laboratory Rover: Wavelength coverage and imaging strategies at the Gale Crater field site, *Lunar Planet. Sci. Conf.*, *43rd*, Abstract #2541.

Bell, J. F., III, et al. (2013), Initial multispectral imaging results from the Mars Science Laboratory Mastcam investigation at the Gale Crater field site, *Lunar Planet. Sci. Conf.*, *44th*, Abstract #1417.

Benn, D. I. (2004), Clast morphology, in *A Practical Guide to the Study of Glacial Sediments*, edited by D. J. A. Evans and D. I. Benn, Oxford Univ. Press, London, pp. 78–92 .

Bibring, J. P., Y. Langevin, J. F. Mustard, F. Poulet, R. Arvidson, and A. Gendrin (2006), Global mineralogical and aqueous Mars history derived from OMEGA/Mars Express data, *Science*, *312*(5772), 400–404, doi:10.1126/science.1122659.

Bockheim, J. G. (2010), Evolution of desert pavements and the vesicular layer in soils of the Transantarctic Mountains, *Geomorphology*, *118*, 433–443.

Bridges, N. T., R. Greeley, A. F. C. Haldemann, K. E. Herkenhoff, M. Kraft, T. J. Parker, and A. W. Ward (1999), Ventifacts at the Pathfinder landing site, *J. Geophys. Res.*, *104*, 8595–8615.

Bridges, N. T., S. Le Mouélic, Y. Langevin, K. E. Herkenhoff, S. Maurice, P. Pinet, R. C. Wiens, M. A. de Pablo, N. O. Rennó, and the MSL Science Team (2013), Rock abrasion textures seen by the ChemCam Remote Microimager on MSL, *Lunar Planet. Sci. Conf.*, *44th*, Abstract #1214.

Bunte, K., and S. R. Abt (2001), Sampling surface and subsurface particle-size distributions in the Wadable gravel and cobble bed streams for analysis in sediment transport, hydraulics, and streambed monitoring, General Technical Report RMRS-GTR-74, Fort Collins, CO: U.S. Department of Agriculture, Forest Service, Rocky Mountain Research Station. 428 p.

Cabrol, N. A., J. D. Farmer, E. A. Grin, L. Richter, L. Soderblom, R. Li, K. Herkenhoff, G. A. Landis, and R. E. Arvidson (2006), Aqueous processes at Gusev Crater inferred from physical properties of rocks and soils along the Spirit traverse, *J. Geophys. Res.*, *111*, E02S20, doi:10.1029/2005JE002490.

Cabrol, N. A., et al. (2008), Soil sedimentology at Gusev Crater from Columbia Memorial Station to Winter Haven, *J. Geophys. Res.*, *113*, E06S05, doi:10.1029/2007JE002953.

Calef, F. J., III, et al. (2013), Geologic mapping of the Mars Science Laboratory landing ellipse, *Lunar Planet. Sci. Conf.*, *44th*, Abstract #2511.

Christensen, P. R., and S. W. Ruff (2004), Formation of the hematite bearing unit in Meridiani Planum: Evidence for deposition in standing water, *J. Geophys. Res.*, *109*, E08003, doi:10.1029/2003JE002233.

Christensen, P. R., R. V. Morris, M. D. Lane, J. L. Bandfield, and M. C. Malin (2001), Global mapping of Martian hematite deposits: Remnants of water-driven processes on early Mars, *J. Geophys. Res.*, *106*(E10), 23,873–23,886.

Dufour, C., et al. (2010), Determination of the first level image processing of the ChemCam RMI instrument for the Mars Science Laboratory (MSL) rover, *International Conference on Space Optics*, October 4–8, 2010, Rhodes, Greece.

Edgett, K. S., et al. (2012), Curiosity's Mars Hand Lens Imager (MAHLI) investigation, *Space Sci. Rev.*, *170*(1–4), 259–317, doi:10.1007/s11214-012-9910-4.

Fenton, L. K., J. L. Bandfield, and A. W. Ward (2003), Aeolian processes in Proctor Crater on Mars: Sedimentary history as analyzed from multiple data sets, *J. Geophys. Res.*, *108*(E12), 5129, doi:10.1029/2002JE002015.

Fergason, R. L., P. R. Christensen, M. P. Golombek, and T. J. Parker (2012), Surface properties of the Mars Science Laboratory candidate landing sites: Characterization from orbit and predictions, *Space Sci. Rev.*, *170*(1–4), 739–773, doi:10.1007/s11214-012-9891-3.

Folk, R. L. (1974), *Petrology of Sedimentary Rocks*, Hemphills Publishing, Austin TX, pp. 170.

Folk, R. L., and W. C. Ward (1957), Brazos River bar: A study in the significance of grain size parameters, *J. Sed. Pet.*, *27*(1), 3–26.

Friday, M. E., C. M. Fedo, I. O. McGlynn, and H. Y. McSween (2013), The accuracy of 2D assessment of sediment textures, and application to Mars, *Lunar Planet. Sci. Conf.*, Abstract #2361.

Furniss, G., J. F. Rittel, and D. Winston (1998), Gas bubble and expansion crack origin of molar-tooth calcite structures in the Middle Proterozoic Belt Supergroup, western Montana, *J. Sed. Res.*, *68*, 104–114, doi:10.2110/jsr.68.104.

Garvin, J. B., P. J. Mouginis-Mark, and J. W. Head (1981a), Characterization of rock populations on planetary surfaces: Techniques and a preliminary analysis of Mars and Venus, *Moon Planets*, *34*, 355–386.

Garvin, J. B., et al. (1981b), Characterization of rock populations on the surfaces of Mars, Venus and Earth: A summary, Abstracts of Papers presented to the Third International Colloquium on Mars, co-sponsored by NASA, LPI, and the Division of Planetary Sciences of the AAS. LPI Contribution 441, published by the Lunar and Planetary Institute, Houston, TX, p.87-90.

Garvin, J. B., J. W. Head, M. T. Zuber, and P. Helfenstein (1984), Venus: The nature of the surface from the Venera panoramas, *J. Geophys. Res.*, *89*(B5), 3381–3399.

Gellert, R., R. Rieder, J. Brückner, B. C. Clark, G. Dreibus, G. Klingelhöfer, G. Lugmair, D. W. Ming, H. Wänke, and S. W. Squyres (2006), Alpha Particle X-Ray Spectrometer (APXS): Results from Gusev crater and calibration report, *J. Geophys. Res.*, *111*, E02S05, doi:10.1029/2005JE002555.

Golombek, M., et al. (2012), Selection of the Mars Science Laboratory landing site, *Space Sci. Rev.*, *170*(1–4), 641–737, doi:10.1007/s11214-012-9916-y.

Grant, F. D., J. D. Farmer, and the Athena Science Team (2005), Spirit's traverse to the Columbia Hills: Systematic variations in clast morphology of pebble to cobble-sized clasts, with implications for geological processes and history, *Geological Society of America*, *Abstracts with Programs*, 37, 7, p. 511.

Grant, J. A., S. A. Wilson, S. W. Ruff, M. P. Golombek, and D. L. Koestler (2006), Distribution of rocks on the Gusev Plains and on Husband Hill, Mars, *Geophys. Res. Lett.*, *33*, L16202, doi:10.1029/2006GL026964.

Grant, J. A., M. P. Golombek, J. P. Grotzinger, S. A. Wilson, M. M. Watkins, A. R. Vasavada, J. L. Griffes, and T. J. Parker (2011), The science process for selecting the landing site for the 2011 Mars Science Laboratory, *Planet. Space Sci.*, *59*, 1114–1127, doi:10.1016/j.pss.2010.06.016.

Grant, J., S. P. Wilson, F. Calef, and MSL Science Team (2013), The relative timing of alluvial activity in Gale Crater, Mars, *Geol. Soc. Am. Abstr. Programs*, *45*, 37 pp.

Greeley, R., et al. (2006), Wind-related features and processes observed by the Mars Exploration Rover Spirit, *J. Geophys. Res.*, *111*, E02S09, doi:10.1029/2005JE002491.

Grin, E. A., and N. A. Cabrol (1997), Limnologic analysis of Gusev crater paleolake, Mars, *Icarus*, *130*, 461–474.

Grotzinger, J. P., and R. E. Milliken (2012), The sedimentary rock record of Mars: Distribution, origins, and global stratigraphy, *SEPM Spec. Pub.*, *102*, 1–48.

Grotzinger, J. P., et al. (2012), Mars Science Laboratory mission and science investigation, *Space Sci. Rev.*, *170*(1–4), 5–56, doi:10.1007/s11214-009-9892-2.

Howard, J. L. (1992), An evaluation of shape indices as palaeoenvironmental indicators using quartzite and metavolcanic clasts in Upper Cretaceous to Palaeogene beach, river and submarine fan conglomerates, *Sedimentology*, *39*, 471–486, doi:10.1111/j.1365-3091.1992.tb02128.x.

Inman, D. L. (1952), Measures for describing the size distribution of sediments, *J. Sed. Pet.*, *22*, 125–145.

Krumbein, W. C., and L. L. Sloss (1963), *Stratigraphy and Sedimentation*, W. H. Freeman, San Francisco, Calif, pp. 106–122.

Laity, J. E. (2009), Landforms, landscapes, and processes of aeolian erosion, in *Geomorphology of Desert Environments*, edited by A. D. Abrahams and A. J. Parsons, Chapman & Hall, London, pp. 597–627.

Laity, J. E., and N. T. Bridges (2009), Ventifacts on Earth and Mars: Analytical, field, and laboratory studies supporting sand abrasion and windward feature development, *Geomorphology*, *105*, 202–217.

Langevin, Y., B. Gondet, S. Le Mouélic, O. Gasnault, K. Herkenhoff, D. Blaney, S. Maurice, R. Wiens, and the MSL Science Team (2013), Processing approaches for optimal science exploitation of the ChemCam Remote Microscopic Imager (RMI) during the first 90 days of Curiosity operations, *Lunar Planet. Sci. Conf., 44th*, Abstract #1227.

Le Mouélic S., et al. (2013), Mars imaging by the ChemCam remote microscopic imager (RMI) onboard Curiosity: The first three months, *Lunar Planet. Sci. Conf., 44th*, Abstract #1213.

Malin, M. C. (1988), Rock populations as indicators of geologic processes (abstract), in Reports of the Planetary Geology and Geophysics Program–1988, NASA Tech. Memo, TM 4041, 502–505.

Malin, M. C. (1989), Rock populations as indicators of geologic processes (abstract), in Reports of the Planetary Geology and Geophysics Program–1989, NASA Tech. Memo., TM 441420, 363–365.

Malin, M. C., and K. S. Edgett (2000), Sedimentary rocks of early Mars, *Science*, *290*(5498), 1927–1937, doi:10.1126/science.290.5498.1927.

Malin, M. C., et al. (2009), The Mars Science Laboratory (MSL) Mars Descent Imager (MARDI) flight instrument, *Lunar Planet. Sci. Conf., 40th*, Abstract #1199.

Malin, M. C., et al. (2010), The Mars Science Laboratory (MSL) Mast-Mounted Cameras (Mastcams) flight instruments, *Lunar Planet. Sci. Conf, 41st*, Abstract #1123.

Maurice, S., R. C. Wiens, M. Saccoccio, B. Barraclough, O. Gasnault, and O. Forni (2012), The ChemCam instrument suite on the Mars Science Laboratory (MSL) rover: Science objectives and mast unit description, *Space Sci. Rev.*, *170*(1–4), 95–166.

Meslin, P.-Y., et al. (2013), Soil diversity and hydration as observed by ChemCam at Gale Crater, Mars, *Science*, *341*(6153), doi:10.1126/science.1238670.

Miall, A. D. (1970), Devonian alluvial fans, Prince of Wales Island, arctic Canada, *J. Sed.. Pet.*, *40*, 556–571.

Milam, K. A., K. R. Stockstill, J. E. Moersch, H. Y. McSween, M. B. Wyatt, and P. R. Christensen (2003), THEMIS characterization of the MER Gusev Crater landing site, *J. Geophys. Res.*, *108*(E12), 8078, doi:10.1029/2002JE002023.

Milliken, R. E., J. P. Grotzinger, and B. J. Thomson (2010), Paleoclimate of Mars as captured by the stratigraphic record in Gale Crater, *Geophys. Res. Let.*, *37*, L04201, doi:10.1029/2009GL041870.

Ming, D. W., et al. (2008), Geochemical properties of rocks and soils in Gusev Crater, Mars: Results of the Alpha Particle X-Ray Spectrometer from Cumberland Ridge to Home Plate, *J. Geophys. Res.*, *113*, E12S39, doi:10.1029/2008JE003195.

Moore, H. J., R. E. Hutton, G. D. Clow, and C. R. Spitzer (1987), Physical properties of the surface materials at the Viking landing sites on Mars: U.S. Geological Survey Professional Paper 1389, 222 pp.

Ollila, A. M., et al. (2013), Early results from Gale Crater on ChemCam detections of carbon, lithium, and rubidium, *Lunar Planet. Sci. Conf., 44th*, Abstract #2188.

Palucis, M. C., W. E. Dietrich, A. Hayes, R. M. E. Williams, F. Calef, D. Y. Sumner, S. Gupta, and C. Hardgrove (2013), Origin and evolution of the Peace Vallis Fan system that drains into the Curiosity landing area, Gale Crater, *Lunar Planet. Sci. Conf., 44th*, Abstract #1607.

Pelkey, S. M., and B. M. Jakosky (2002), Surficial geologic surveys of Gale Crater and Melas Chasma, Mars: Integration of remote-sensing data, *Icarus*, *160*(2), 228–257, doi:10.1006/icar.2002.6978.

Piqueux, S., and P. R. Christensen (2009), A model of thermal conductivity for planetary soils: 2. Theory for cemented soils, *J. Geophys. Res.*, *114*, E09006, doi:10.1029/2008JE003309.

Pollock, M. D., L. C. Kah, and J. K. Bartley (2006), Morphology of molar-tooth structures in Precambrian carbonates: Influence of substrate rheology and implications for genesis. *J. Sed. Res.*, *76*, 310323, doi:10.2110/jsr.2006.021.

Presley, M. A., and P. R. Christensen (1997), Thermal conductivity measurements of particulate materials 2. Results, *J. Geophys. Res.*, *102*(E3), 6551–6566, doi:10.1029/96JE03303.

Putzig, N. E., and M. T. Mellon (2007a), Thermal behavior of horizontally mixed surfaces on Mars, *Icarus*, *191*, 52, doi:10.1016/j.icarus.2007.03.022.

Putzig, N. E., and M. T. Mellon (2007b), Apparent thermal inertia and the surface heterogeneity of Mars, *Icarus*, *191*, 68–94.

Rogers, A. D., and J. L. Bandfield (2009), Mineralogical characterization of Mars Science Laboratory candidate landing sites from THEMIS and TES data, *Icarus*, *203*(2), 437–453.

Sautter, V., et al. (2013), Is Bathurst Inlet rock an evidence of explosive volcanism in the Rocknest area of Gale Crater?, *Lunar Planet. Sci. Conf., 44th*, Abstract #1985.

Schieber, J., M. C. Malin, T. Olson, K. Edgett, M. T. Lemmon, and K. Comeaux (2013), Blowing dust and flying pebbles: An analysis of MARDI images for rocket-induced sediment movement, this volume.

Schmidt, M. E., et al. (2013), APXS of first rocks encountered by Curiosity in Gale Crater: Geochemical diversity and volatile element (K and Zn) enrichment, *Lunar Planet. Sci. Conf., 44th*, Abstract #1278.

Siebach, K. L., and J. P. Grotzinger (2013), Formation of boxwork structures on Mount Sharp, Gale Crater, Mars, *Lunar Planet. Sci. Conf., 44th*, Abstract #1875.

Stolper, E. M., et al. (2013), The petrochemistry of Jake_M: A Martian mugearite, *Lunar Planet. Sci. Conf., 44th*, Abstract #1685.

Sullivan, R. D., et al. (2005), Aeolian processes at the Mars Exploration Rover Meridiani Planum landing site, *Nature*, *436*, doi:10.1029/nature03641.

Summons, R. E., J. P. Amend, D. Bish, R. Buick, G. D. Cody, D. J. Des Marais, G. Dromart, J. L. Eigenbrode, A. H. Knoll, and D. Y. Sumner (2011), Preservation of Martian organic and environmental records: Final report of the Mars Biosignature Working Group, *Astrobiology*, *11*, 157–181, doi:10.1089/ast.2010.0506.

Sumner, D. Y., et al. (2013), Preliminary geological map of the Peace Vallis fan integrated with in situ mosaics from the Curiosity rover, Gale Crater, Mars, *Lunar Planet. Sci. Conf., 44th*, Abstract #1699.

Thomson, B. J., N. T. Bridges, and R. Greeley (2008), Rock abrasion features in the Columbia Hills, Mars, *J. Geophys. Res.*, *113*, E08010, doi:10.1029/2007JE003018.

Thomson, B. J., N. T. Bridges, R. Milliken, A. Baldridge, S. J. Hook, J. K. Crowley, G. M. Marion, C. R. de Souza Filho, A. J. Brown, and C. M. Weitz (2012), Constraints on the origin and evolution of the layered mound in Gale Crater, Mars using Mars Reconnaissance Orbiter data, *Icarus*, *214*, 413–432, doi:10.1016/j.icarus.2011.05.002.

Wentworth, C. K. (1922), A scale of grade and class terms for clastic sediments, *J. Geol.*, *30*, 377–392.

Wiens, R. C., et al. (2013), Compositions determined by ChemCam along Curiosity's traverse from Bradbury Station to Glenelg in Gale Crater, Mars. Lunar Planet. Sci. LXIV, 1363.

Williams, R. M. E., et al. (2013), Martian fluvial conglomerates at Gale Crater, *Science*, *340*(6136), 1068–1072, doi:10.1126/science.1237317.

Wray, J. J. (2013), Gale Crater: The Mars Science Laboratory/Curiosity Rover landing site, *Int. J. Astrobiology*, *12*, 25–38, doi:10.1017/S1473550412000328.

Yingst, R. A. (2009), Mars Analog Handlens-scale image database, residing on the PDS geosciences node at: http://pds-geosciences.wustl.edu/missions/labdata/marshandlens.htm.

Yingst, R. A., A. F. C. Haldemann, K. L. Biedermann, and A. M. Monhead (2007), Quantitative morphology of rocks at the Mars Pathfinder landing site, *J. Geophys. Res.*, *112*, E06002, doi:10.1029/2005JE002582.

Yingst, R. A., L. Crumpler, W. H. Farrand, R. Li, N. A. Cabrol, and L. D. Neakrase (2008), Morphology and texture of particles along the Spirit rover traverse from sol 450 to sol 745, *J. Geophys. Res.*, *113*, E12S41, doi:10.1029/2008JE003179.

Yingst, R. A., et al. (2013), Characteristics of pebble and cobble-sized clasts along the Curiosity rover traverse from sol 0 to 90, *LPSC, 44th*, Abs. #1232.